JGR Solid Earth

RESEARCH ARTICLE
10.1029/2022JB024354

Special Section:
Understanding and anticipating Induced Seismicity: from mechanics to seismology

Limited Earthquake Interaction During a Geothermal Hydraulic Stimulation in Helsinki, Finland

Grzegorz Kwiatek[1], Patricia Martínez-Garzón[1], Jörn Davidsen[2,3], Peter Malin[4], Aino Karjalainen[5], Marco Bohnhoff[1,6], and Georg Dresen[1,7]

[1]Section 4.2 Geomechanics and Scientific Drilling, Helmholtz Centre Potsdam, GFZ German Research Centre for Geosciences, Potsdam, Germany, [2]Complexity Science Group, Department of Physics and Astronomy, University of Calgary, Calgary, AB, Canada, [3]Hotchkiss Brain Institute, University of Calgary, Calgary, AB, Canada, [4]ASIR Advanced Seismic Instrumentation and Research, Dallas, TX, USA, [5]St1 Oy, Helsinki, Finland, [6]Department of Earth Sciences, Institute of Geological Sciences, Free University Berlin, Berlin, Germany, [7]Institute of Earth and Environmental Science, University of Potsdam, Potsdam, Germany

Key Points:

- Induced seismicity associated with stimulation campaign in a 5.8 km deep geothermal OTN-2 well passively responds to injection operations
- Seismicity is a non-stationary Poisson process with seismicity rate and maximum magnitude modulated by the hydraulic energy input rate
- Seismicity clusters in space and time in response to fluid injection but no interaction between earthquakes is observed

Supporting Information:

Supporting Information may be found in the online version of this article.

Correspondence to:

G. Kwiatek,
kwiatek@gfz-potsdam.de

Citation:

Kwiatek, G., Martínez-Garzón, P., Davidsen, J., Malin, P., Karjalainen, A., Bohnhoff, M., & Dresen, G. (2022). Limited earthquake interaction during a geothermal hydraulic stimulation in Helsinki, Finland. *Journal of Geophysical Research: Solid Earth*, *127*, e2022JB024354. https://doi.org/10.1029/2022JB024354

Received 9 MAR 2022
Accepted 5 SEP 2022

Author Contributions:

Conceptualization: Grzegorz Kwiatek
Formal analysis: Grzegorz Kwiatek, Patricia Martínez-Garzón, Jörn Davidsen
Investigation: Grzegorz Kwiatek, Patricia Martínez-Garzón, Jörn Davidsen
Methodology: Grzegorz Kwiatek
Resources: Aino Karjalainen

Abstract We investigate induced seismicity associated with a hydraulic stimulation campaign performed in 2020 in the 5.8 km deep geothermal OTN-2 well near Helsinki, Finland as part of the St1 Deep Heat project. A total of 2,875 m^3 of fresh water was injected during 16 days at well-head pressures <70 MPa and with flow rates between 400 and 1,000 L/min. The seismicity was monitored using a high-resolution seismic network composed of 10 borehole geophones surrounding the project site and a borehole array of 10 geophones located in adjacent OTN-3 well. A total of 6,121 induced earthquakes with local magnitudes $M_L^{Hel} > -1.9$ were recorded during and after the stimulation campaign. The analyzed statistical parameters include magnitude-frequency *b*-value, interevent time and interevent time ratio, as well as magnitude correlations. We find that the *b*-value remained stationary for the entire injection period suggesting limited stress build-up or limited fracture network coalescence in the reservoir. The seismicity during the stimulation neither shows signatures of magnitude correlations, nor temporal clustering or anticlustering beyond those arising from varying injection rates. The interevent time statistics are characterized by a Poissonian time-varying distribution. The calculated parameters indicate no earthquake interaction. Focal mechanisms suggest that the injection activated a spatially distributed network of similarly oriented fractures. The seismicity displays stable behavior with no signatures pointing toward a runaway event. The cumulative seismic moment is proportional to the cumulative hydraulic energy and the maximum magnitude is controlled by injection rate. The performed study provides a base for implementation of time-dependent probabilistic seismic hazard assessment for the project site.

Plain Language Summary We investigate anthropogenic seismicity associated with fluid injection into the 5.8 km deep geothermal OTN-2 well near Helsinki, Finland, as a part of St1 Deep Heat Project. A total of 2,875 m^3 of fresh water was injected during 16 days at well-head pressures <70 MPa and with flow rates between 400 and 1,000 L/min. The seismicity was monitored using a seismic network composed of 20 borehole geophones located in Helsinki area and in the OTN-3 well located close by the injection site. A total of 6,121 earthquakes indicating fractures of 1–30 m size were recorded during and after stimulation campaign. Using a handful of statistical properties derived from earthquake catalog we found no indication for earthquakes being triggered by other earthquakes. Instead, the earthquake activity rates, as well as the maximum earthquake size stayed proportional to the fluid injection rate. The spatio-temporal behavior of seismicity and its properties suggest earthquakes occurred not on a single fault, but in a distributed network of similarly oriented fractures, limiting the possibility for occurrence of violent earthquakes. The performed study provides evidence that the induced seismicity due to injection performed within St1 Deep Heat project is stable and allow to constrain seismic hazard.

1. Introduction

Geothermal energy is considered an important and growing source of low-carbon-footprint energy. Development of deep Enhanced Geothermal Systems (EGS) using massive fluid injection (hydraulic fracturing) to improve reservoir permeability often leads to the occurrence of induced seismicity (e.g., Majer et al., 2012). Large earthquakes associated with anthropogenic fluid injection activities such as in Basel, Switzerland (e.g., Giardini, 2009)

Supervision: Georg Dresen
Validation: Grzegorz Kwiatek, Patricia Martínez-Garzón
Visualization: Grzegorz Kwiatek
Writing – original draft: Grzegorz Kwiatek
Writing – review & editing: Patricia Martínez-Garzón, Jörn Davidsen, Peter Malin, Aino Karjalainen, Marco Bohnhoff, Georg Dresen

or Pohang, South Korea (e.g., Hofmann et al., 2019) had a vast negative socio-economic impact and lead to the shutdown of the respective geothermal projects. Successful mitigation of seismic hazard is crucial from the operational point of view, as well as for the public acceptance of future geothermal projects.

Seismic hazard associated with fluid injection in the subsurface requires much better understanding of the factors governing the seismic energy release in response to the injection protocol (injection rate, injection pressure, and hydraulic energy) and local site conditions (fault inventory, state of stress, and local geology). Recently developed models provide an estimate of maximum earthquake magnitude related to fluid injection for a *stable*, pressure-controlled phase of fluid injection, where the total seismic moment release and maximum magnitude are related to injected fluid volume, while other factors such as pumping rate and reservoir structure. For example, McGarr (2014) proposed that total seismic moment release (the static deformation caused by earthquakes) and maximum event magnitude increase linearly with total volume of fluid injected, $M_0^{\max} \propto V^1$, $\sum M_0 \propto V^1$, or alternatively to the *volume of rock mass perturbed by fluid injection* $V^{\text{perturbed}}$ and average pore pressure increase in that volume, $M_0^{\max} \propto V^{\text{perturbed}} \Delta P$ (cf. Kwiatek et al., 2015; Martínez-Garzón et al., 2020). The fracture mechanics-based model of Galis et al. (2017) provided estimates of the maximum magnitude of self-arrested ruptures increasing nonlinearly with total fluid volume, $M_0^{\max} \propto V^{3/2}$. Using the seismogenic index concept (e.g., Shapiro et al., 2010), van der Elst et al. (2016) related injected fluid volume to seismic activity, total seismic moment release and maximum magnitude, with $M_0^{\max} \propto V^{3/2}$ for a Gutenberg-Richter *b*-value of 1. Based on a recent conceptual model (Lord-May et al., 2020) one can generalize the relation between injected fluid volume, magnitude-frequency distribution and resulting seismic hazard, which depends on the loading history arising from both fluid injections and natural aseismic loading as well as on the heterogeneity of the host medium.

As already indicated, most of the proposed models of increasing $M_0^{\max}$ with injected V are limited to a *stable*, pressure-controlled regime but do not capture a potential transition to an *unstable* or *runaway* rupture (see e.g., discussion in Kroll & Cochran, 2021). Such an unstable event may affect the entire length and width of tectonic faults within or near the stimulated reservoir. Bentz et al. (2020) compiled numerous studies of fluid-induced seismicity and showed that most of the analyzed enhanced geothermal systems displayed, after some period of time, a prolonged, *stable* period of seismic energy E_0 (or seismic moment M_0) release proportional to the hydraulic energy input, that is, the time integral of the product of well head pressure and injection rate. These stable periods were observed for reservoirs displaying a wide range of seismic injection efficiencies η^{inj}, where $\eta^{\text{inj}}$is the estimated ratio of seismic E_0 release to hydraulic energy E_H input (e.g., Maxwell, 2011). For these stable injection periods, the estimated radiated seismic energy remained below the maximum event magnitude predicted by the McGarr (2014) model.

Increasing total seismic energy release with total fluid volume was also found in laboratory experiments (Wang, Kwiatek, Rybacki, Bohnhoff, & Dresen, 2020; Wang, Kwiatek, Rybacki, Bonnelye et al., 2020). In contrast to a stable evolution of seismic moment observed for most projects, others displayed seismic moment evolution with progressive injection clearly indicating an unstable energy release. Examples include the Pohang EGS (c.f. Ellsworth et al., 2019) and Cooper Basin EGS (c.f. Baisch, 2020) displaying continuously increasing η^{inj} throughout the injection periods, representing a signature of an emerging failure process leading to *runaway* rupture.

The transition toward unstable failure in an otherwise *stable*, pressure-controlled regime is not well understood. The physical mechanisms governing a transition from a stable injection regime into a run-away rupture are still a matter of debate (Wang, Kwiatek, Rybacki, Bohnhoff, & Dresen, 2020; Wang, Kwiatek, Rybacki, Bonnelye et al., 2020). This transition could be governed by total injected fluid volume (Galis et al., 2017) or pressure build-up and injection rate (Alghannam & Juanes, 2020; Rudnicki & Zhan, 2020; Wang, Kwiatek, Rybacki, Bohnhoff, & Dresen, 2020; Wang, Kwiatek, Rybacki, Bonnelye et al., 2020). Site conditions, including background stress level and its orientation with respect to a local fault or fault network, in addition to elevated pore fluid pressures may promote stress transfer between events (earthquake interactions, aftershock or triggering processes, see e.g., Cochran et al., 2020; Verdeccia et al., 2021 and references therein for details). That is to say that there are several critical factors that may contribute to induced seismic activity and the occurrence of large earthquakes.

It is still a matter of debate to what extent earthquake interaction affect the evolution of induced seismicity activity. A fluid-induced and pressure-controlled earthquake sequence may be modeled by a random *Poisson* process (e.g., Langenbruch et al., 2011), where successively occurring events are not causally related to each other ("background seismicity"). The observed total number of seismic events as well as seismicity rates can

be successfully reproduced assuming a fluid pressure perturbation and free model parameters such as friction or cohesion (Gischig & Wiemer, 2013). In contrast, Catalli et al. (2013, 2016) showed that static stress transfer between induced earthquakes may in fact play a significant role in triggering earthquakes in EGS stimulation campaigns, especially toward the end of injection. Schoenball et al. (2012) investigated seismicity recorded in the Soultz-sous-Forets EGS project. They found that static stress changes may vary considerably on a local scale, promoting local earthquake interactions. This agrees with analysis of acoustic emission events during rock deformation laboratory stick-slip experiments, where local stress concentrations caused by defects (inclusions and notches), rather than global stress level, were found to control event-event triggering (Davidsen et al., 2021; Meredith & Atkinson, 1983). Schoenball et al. (2012) found that triggering by static stress transfer plays a minor role in reservoirs for which deformation is distributed over a certain volume, but may lead to interacting events within a single and prominent fault zone. Martínez-Garzón et al. (2018) studied the clustering and triggering properties of three geothermal reservoirs in California, USA. They found increased earthquake triggering during periods of high injection rates (i.e., stressing rates). They also noted that reservoir structure and ambient stress state affected the rate of background seismicity. Yeo et al. (2020) studied seismicity associated with fluid injection in Pohang, South Korea. They found that cumulative Coulomb stress changes from small earthquakes on a single fault are in the range of stress changes due to pore pressure changes, suggesting that large induced events may drive seismicity leading to the occurrence of large earthquakes. Finally, Catalli et al. (2016) and Brown and Ge (2018) highlighted the importance of stress transfer between seismic events for earthquake forecasting and seismic hazard assessment. Brown and Ge (2018) recommended mitigation actions if seismic analysis indicates stress transfer and triggering, in particular in the absence of fluid injection.

In June–July 2018, a total volume of 18,160 m^3 of water was injected into the crystalline basement during a first stimulation campaign performed in the St1 Deep Heat project in Helsinki, Finland (Ader et al., 2019; Hillers et al., 2020; Kwiatek et al., 2019; Leonhardt, Kwiatek, Martínez-Garzón, et al., 2021). The injection schedule was adopted in a feedback traffic light-system in response to near-real-time seismic monitoring of induced seismicity rates, hypocenter locations and magnitudes, and evolution of seismic and hydraulic energy (Kwiatek et al., 2019). This adaptive stimulation approach allowed to avoid the occurrence of a "red alert" seismic event with a moment magnitude above M_W 2.0, which was a limit set by the local authorities.

In this study we analyze the induced seismicity associated with a follow-up stimulation campaign performed in May 2020 (Rintamäki et al., 2021). We first develop a high-resolution seismicity catalog and then analyze the seismic activity in response to the injection operations in 2020 and compare it to the previous massive stimulation campaign in June–August 2018 (e.g., Kwiatek et al., 2019). We calculate statistical and spatio-temporal properties of the induced seismicity in response to injection operations performed at the site, with a special focus on parameters signifying potential earthquake interactions. We then discuss the implications of our observations for seismic response of a stimulated geothermal reservoir (stable and pressure-controlled evolution of seismic moment vs. run-away ruptures) and local seismic hazard. Our study highlights that high-frequency low-magnitude monitoring and near-real-time analysis of seismic data, combined with analysis of the reservoir structure and local stress conditions are prerequisite in attempts to successfully control induced seismicity in the St1 Deep Heat project and other comparable deep geothermal systems.

2. Data and Methods

2.1. Project Site

The St1 Deep Heat project site is located on the Aalto University campus in Helsinki, Finland. (Figure 1) (Kwiatek et al., 2019). Two separate deep injection wells (OTN-2 and OTN-3) were drilled into Precambrian basement rocks consisting of granites, pegmatites, gneisses, and amphibolites covered by quaternary deposits typically with <20 m thickness (see Kwiatek et al., 2019 for details). Due to their long geological history, basement rocks display complex tectonics including folds, faults joints and foliation. The deeper well OTN-3 reached 6,400 m measured depth (6,087 m b.s.l., 6,100 m of overburden) with an open-hole section of 1,000 m inclined at 45° toward NE (Figures 1b and 1c). The well was stimulated in five injection inflatable packer-separated stages in June and July 2018. The general project, the 2018 stimulation campaign as well as the associated seismicity analysis are described in detail in Kwiatek et al. (2019), as well as in Ader et al. (2019); Hillers et al. (2020); Leonhardt, Kwiatek, Martínez-Garzón, et al. (2021). Between late 2019 and Spring 2020, the existing shallower well OTN-2 was deepened to the final depth of 5,765 m b.s.l. with a deviated bottom open-hole section parallel to

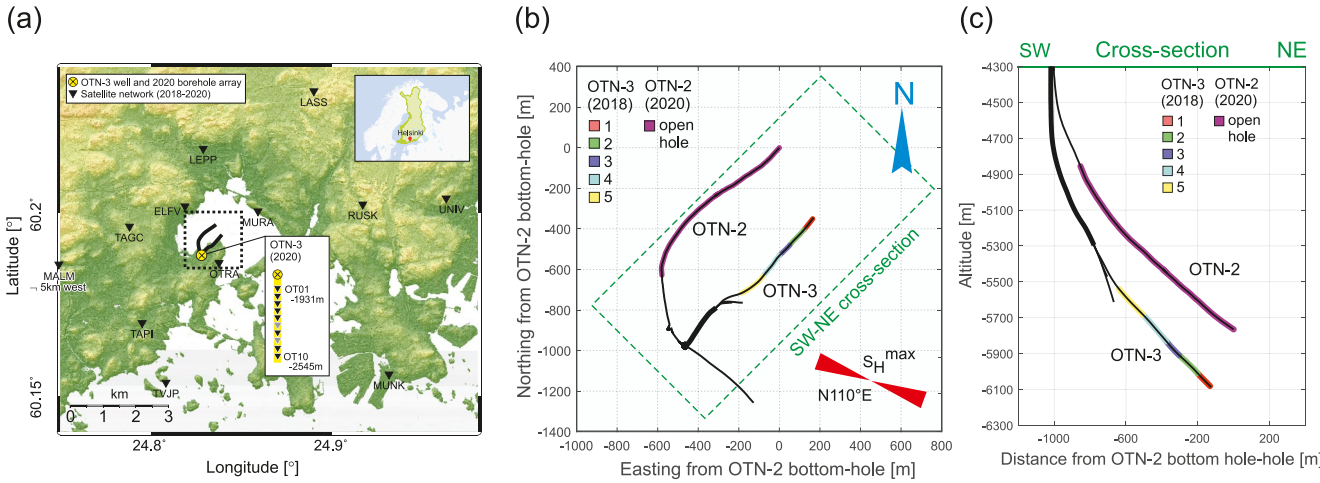

Figure 1. (a): Overview of the St1 Deep Heat project site in Helsinki/Finland and the status of the downhole seismic monitoring network during the 2020 OTN-2 stimulation. Black reverted triangles denote individual borehole geophones (depth range 238–1,133 m b.s.l.) and slots of a vertical array in the well OTN-3 (depth range 1,931–2,545 m b.s.l.). Gray sensors within the vertical array were not used in analysis due to enhanced electronic noises; (b): Zoom-in of the dotted rectangle in (a). The 2020 open-hole stimulation interval in the OTN-2 well is shown in magenta. Depth intervals in OTN-3 hydraulically stimulated in 2018 in five packer-separated stages are encoded by five different colors (see Kwiatek et al., 2019 for details); (c): SW-NE depth section seen from SE focused on lowermost portions of the OTN-2 and OTN-3 wells.

the OTN-3 trace starting at 4.9 km depth (Figure 1c). Open-hole sections of both wells are separated laterally by approx. 400 m. Azimuths of both wells are approximately perpendicular to the direction of maximum horizontal stress (see Figure 1b and discussion in Kwiatek et al., 2019).

2.2. OTN-2 Stimulation Campaign in May 2020

The here discussed stimulation campaign was performed between 4 and 20 May 2020. A total of 2,875 m^3 of water were injected into the open-hole section of the OTN-2 well in the depth interval 4,856–5,765 m b.s.l. (Figures 1b and 1c) (Rintamäki et al., 2021) to establish communication between two wells. Similar to the 2018 stimulation campaign performed in well OTN-3, the 2020 stimulation was flow-rate controlled. The maximum well head pressures did not exceed 70 MPa (approx. 25 MPa downhole pressure) and injection rates were kept at a relatively low level of 400 L/min (during 84% of the injection period), with occasional short periods of injection at rates up to 1,000 L/min (Figure 2). The total volume of fluid injected was only about 16% of the 18,000 m^3 injected in 2018. Well head pressures also were substantially below the maximum 90 MPa reached in 2018, where different high-performance pumps were used (c.f. Kwiatek et al., 2019).

2.3. Seismic Monitoring

The near-real-time seismic monitoring network of the 2020 stimulation campaign at OTN-2 was composed of 22 borehole 3C sensors developed and installed by ASIR LLC. The centerpiece was a 10-level borehole sensors array (hereafter called "borehole array") of three-component Geospace OMNI-2,400 geophones (15 Hz natural frequency) sampled at 2 kHz. Compared to the instrumentation used to monitor the 2018 stimulation, the borehole array was modified by removing two sensors and increasing the spacing between the remaining 10 sensors. The refurbished array was placed in the OTN-3 well at 1.93–2.55 km depth. This was close to the location of the borehole array placed in the OTN-2 well at depths 2.20–2.65 km during the campaign in 2018 (see inset in Figure 1a). Additional 12 sensors (hereafter called "satellite network") equipped with three-component short-period 4.5 Hz natural frequency Sunfull PSH geophones completed the monitoring network. These sensors were installed before the 2018 stimulation campaign (Figure 1a) in 0.30–1.13 km deep boreholes surrounding the injection well extending throughout the Helsinki area. The entire monitoring system was fully operational in December 2019, about 5 months before the May 2020 stimulation.

Near-real-time processing of induced seismicity data started on 26 January 2020, that is, about 3 months prior to the onset of the injection. This provided extensive information on the background seismicity around the injection site used for seismic hazard assessment. For the time period including OTN-2 stimulation campaign and 2 weeks

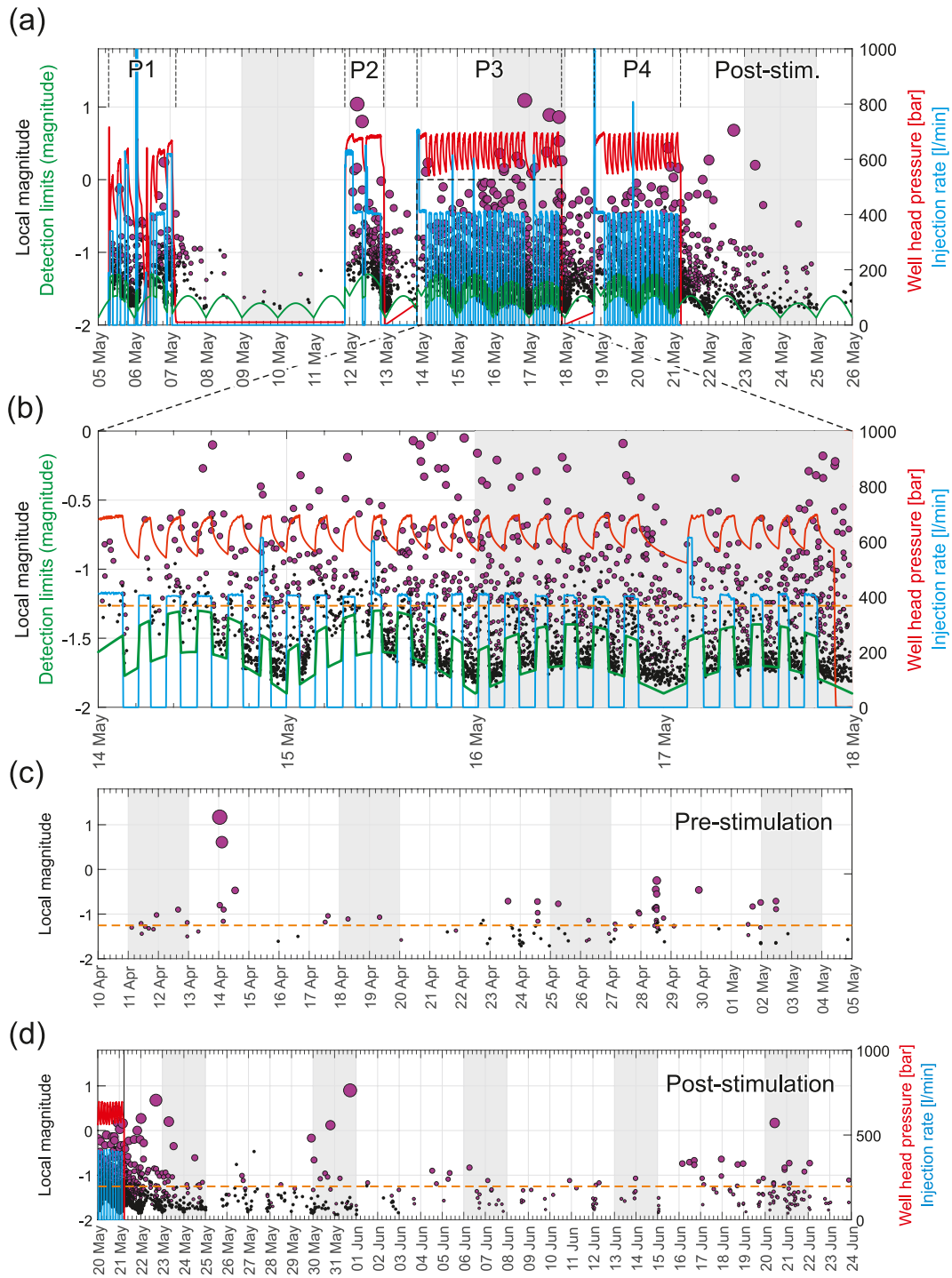

Figure 2. (a): Overview of hydraulic and seismicity parameters for the 2020 OTN-2 stimulation campaign in May 2020. Circles represent local magnitude of detected seismic events. The red and blue solid lines correspond to the OTN-2 well head pressure and injection rate, respectively. Selected time intervals of the injection campaign are labeled P1–P4. The ad-hoc derived fit to the limits to earthquake detection limit (see Text S2 in Supporting Information S1 for details) and conservative magnitude of completeness M_C^* are shown using green solid line and orange dashed lines, respectively (see text for detailed discussion). (b): Zoom-in of time period between May 14th and May 18th days during injection phase P3 of the injection campaign showing fluctuations of the earthquake detection threshold in response to daily urban noise level changes and injection-related noises. Note the slightly improved detection conditions during the weekend period (shaded days); (c) last weeks of seismicity preceding the OTN-2 stimulation campaign; (d) seismicity following the OTN-2 stimulation campaign.

after the stimulation campaign, the seismic data recovery was >99%, allowing for the development of a consistent seismic catalog. Monitoring and processing stopped end of June 2020, about 1 month after the stimulation of the well was completed.

2.4. Seismic Catalog Development

The seismicity catalog provided by the industrial operator initially contained 6,243 event detections including mostly induced earthquakes, but also electronic noises and signals originating from or near the surface. To refine the catalog, we first included additional events (detections) that were only recorded by the deep OTN-3 array. To optimize detections of missing induced seismic events from within the stimulated reservoir, a coincidence trigger was run on the database of remaining P-wave arrivals only observed at stations forming the OTN-3 array. The remaining P-arrivals observe on the OTN-3 borehole array stations were matched with that predicted and observed for earthquakes located within located clusters (see details of the procedure in Kwiatek et al., 2019; Leonhardt, Kwiatek, Martínez-Garzón, et al., 2021). This enhanced the initial catalog by 3,720 newly detected events to a total of 9,963 detected events.

Then we performed an automated inspection of observed hodographs by comparing the observed patterns of P-and S-wave arrivals on sensors forming the OTN-3 array with those predicted for events occurring nearby the OTN-2 injection volume (defined as cube of $2 \times 2 \times 2$ km^3 centered at the injection interval). This allowed to confirm that 6,318 events out of the 9,963 detected events originate from the stimulated reservoir. The remaining 3,645 events were manually inspected. It turned out they are transient signals of mechanical (low frequency) or electronic (high frequency) origin or seismic events related to surface blasting and soil compaction works performed in well-identified areas surrounding the project site (3–7 km away).

The vast majority of the 6,318 confirmed induced seismic events were only visible on seismograms from sensors of the OTN-3 borehole array. Using clearly visible P-and S-wave arrivals, the distance between induced earthquakes from OTN-3 array sensors as well as event magnitudes could be well estimated (see next section). Local "Helsinki" (Uski et al., 2015; Uski & Tuppurainen, 1996) magnitudes ranging from $M_{\mathrm{L}}^{\mathrm{Hel}}$ −1.5 to $M_{\mathrm{L}}^{\mathrm{Hel}}$ 1.2 could be then calculated for all 6,318 seismic events.

To locate the seismic events, we used the Equivalent Differential Time method (Font et al., 2004) as in previous studies (Kwiatek et al., 2019; Leonhardt, Kwiatek, Martínez-Garzón, et al., 2021). We used a 1D P-wave velocity model based on a vertical seismic profiling campaign (Leonhardt, Kwiatek, Martínez-Garzón, et al., 2021) assuming a V_P/V_S ratio of 1.71 for inverting S-wave arrival times. The location inverse problem was solved using the Metropolis-Hastings Random Walk algorithm developed in MATLAB (MHRW, Metropolis et al., 1953; Hastings, 1970). Hypocenter locations (x, y, and z) were estimated as a mode from MHRW-sampled empirical probability density distributions of hypocenter locations. However, using the MHRW-derived location uncertainties, we found the accurate hypocentral locations could not be achieved for most events without additional P-and S- phase arrivals from sensors forming the satellite network. This was evidenced by elongated empirical distributions of location uncertainties obtained from MHRW algorithm suggesting a clear lack of sufficient azimuthal coverage due to lack of picks from satellite network. Consequently, only the 72 largest events could be well located using additional P-and S-wave onsets available on sensors forming the satellite network. In the following, these 72 earthquakes were further relocated using the Double-Difference (DD) method (Waldhauser & Ellsworth, 2000). These events and 1,987 events from the earlier 2018 stimulation (Leonhardt, Kwiatek, Martinez-Garzon, & Heikkinen, 2021) of well OTN-3 were relocated jointly. The combined relocation of both catalogs allowed preserving the relative distances between all clusters of seismic events forming the 2018 seismicity and new clusters activated during the 2020 stimulation. For the 2020 stimulation we ultimately relocated 45 events out of initial 72. The relative location precision (95% confidence interval) in horizontal and vertical direction was not exceeding ±85 m and ±42 m, respectively.

2.4.1. Local Magnitude $M_{\mathrm{L}}^{\mathrm{Hel}}$, Seismic Moment M_0, and Radiated Energy E_0

Local magnitude $M_{\mathrm{L}}^{\mathrm{Hel}}$ was calculated following Uski and Tuppurainen (1996) and Uski et al. (2015) using seven selected 3C sensors from the borehole array that displayed the lowest noise across the full frequency band of the seismic recordings. The magnitude has been converted to seismic moment M_0 following the regressive relation

from Uski et al. (2015) (see Text S1 in Supporting Information S1). The seismic moment was directly converted to radiated seismic energy E_0 (Hanks & Kanamori, 1979):

$$E_0 = \Delta\sigma \frac{M_0}{2G}, \tag{1}$$

assuming a stress drop value of $\Delta\sigma = 9$ MPa and a shear modulus of $G = 39$ GPa. We used the average stress drop estimated for 56 events using spectral fitting method (see Kwiatek et al., 2019 for detailed discussion on stress drop estimation).

2.4.2. *b*-Value

The Gutenberg-Richter magnitude-frequency distribution provides information on earthquake occurrence rates for each considered magnitude (Gutenberg, Richter, 1944) in a generic form $\log_{10} N = a - bM$, where N is the number of earthquakes surrounding of magnitude M above some limiting magnitude of completeness M_C. The slope of the magnitude-frequency distribution of events (b-value) and the magnitude of completeness (M_C) have been calculated for the seismic catalog using the maximum likelihood method (Utsu, 1965), including a correction for the histogram bin size (Lasocki & Papadimitriou, 2006), and the goodness of fit method (Wiemer & Wyss, 2000). For the latter, we calculated the b-value assuming that 95% of the events follow a Gutenberg-Richter power law. To investigate the temporal evolution during injection periods, we additionally calculated the b-value in a moving-time window of 250 events. The uncertainties in b-value were estimated following Shi and Bolt (1982) suitable for time varying b-values.

2.4.3. Magnitude Correlations

For selected time periods we tested whether magnitude correlations exist between consecutive events included in the seismic catalog. Magnitude correlations between events would indicate that the events are not independent allowing an improved probabilistic forecast of the magnitude of forthcoming earthquakes beyond simply using the Gutenberg-Richter distribution (Davidsen et al., 2012; Maghsoudi et al., 2016). In particular, we focused on the observed catalog of magnitude differences,

$$\Delta \boldsymbol{M} = [\Delta M_i] = M_{i+1} - M_i, \tag{2}$$

where $[\Delta M_i]$ is the catalog of earthquake magnitude differences exceeding the magnitude of completeness ordered by time. To avoid any potential biases due to catalog incompleteness (Davidsen & Green, 2011), we focus on complete catalogs that only contain events above the magnitude of completeness. The Probability Density Function (PDF) of samples, $p(\Delta \boldsymbol{M})$, is expected to significantly deviate from the distribution of magnitude differences $p(\Delta \mathbf{M}^*)$of uncorrelated magnitudes $\Delta \boldsymbol{M}^* = \left[\Delta \mathrm{M}_i^*\right]$ if a correlation between the magnitudes of consecutive events would exist (e.g., Davidsen et al., 2012). The latter distribution can be obtained by considering $\Delta M_i^* = M_{i^*} - M_i$, where M_i is the ith magnitude in the original catalog of magnitudes and each M_{i^*} is a magnitude randomly drawn from the original (complete) catalog of magnitudes. Hence, the absence of events below the magnitude of completeness does not bias our analysis since this comparative random null model does not take them into account either. This vector of uncorrelated magnitudes can be generated multiple times, allowing to quantify the variability of $p\left(\Delta \boldsymbol{M}^*\right)$ formed from many series realizations of $\left[\Delta M_i^*\right]$. In the following, differences between original cumulative distribution functions (CDFs), $p(\Delta \boldsymbol{M} < \Delta m)$, and CDFs built upon the perturbed vectors of magnitudes are calculated:

$$\delta p(\Delta m) = p(\Delta \boldsymbol{M} < \Delta m) - p\left(\Delta \boldsymbol{M}^* < \Delta m\right). \tag{3}$$

In the absence of magnitude correlations, $\delta p(\Delta m)$ should not significantly deviate from 0 for all considered Δm. This means that the catalog magnitudes are indistinguishable from a sequence randomly generated from the Gutenberg-Richter distribution. In contrast, if the PDF of magnitude differences formed from $\Delta \boldsymbol{M}$ is significantly different from those built upon multiple random permutations of the same catalog, the catalog may display magnitude correlations. Such magnitude correlations could be indicative of earthquake-earthquake interactions but this might not be the only cause. For example, specific geological settings can induce seismic events of similar magnitude giving rise to magnitude correlations (Maghsoudi et al., 2016)—correlations do not necessarily imply causation.

2.4.4. Interevent Time Statistics

To calculate the interevent time statistics, we started from the vector of interevent times calculated from origin times T_i of earthquakes for a complete seismic catalog, ordered in time:

$$\Delta \boldsymbol{T} = [\Delta T_i] = T_{i+1} - T_i, \tag{4}$$

and calculated the corresponding PDF, $p(\Delta \boldsymbol{T}/\langle \Delta T \rangle)$, where $\langle \Delta T \rangle$ is the mean interevent time of the whole sequence containing N elements: $\langle \Delta T \rangle = (T_N - T_1)/(N-1)$. A normalized interevent time distribution indistinguishable from an exponential is expected for a random set of independent events in time corresponding to a stationary Poisson process. Hence, the distribution can provide first-order information on whether the analyzed sequence contains temporal correlations between events, which could indicate earthquake-earthquake interactions and aftershocks, for example.

2.4.5. Interevent Time Ratio

Following van der Elst and Brodsky (2010) the interevent time ratio statistics were calculated using a temporally-ordered seismicity catalog of selected seismic events $\boldsymbol{T} = [T_i]$:

$$\boldsymbol{R} = [R_i] = \frac{T_{i+1} - T_i}{T_{i+1} - T_{i-1}}. \tag{5}$$

In the absence of temporal (anti-)clustering of seismic events (e.g., aftershock or foreshock sequences), that is, for a stationary *or* a time-varying Poisson process, $p(\boldsymbol{R})$ is expected to be characterized by a uniform distribution in the interval $R \in (0, 1)$. Temporal clustering and anti-clustering of seismicity is expressed by statistically significant peaks of $p(\boldsymbol{R})$ observed around 0 and 1, respectively (van der Elst and Brodsky, 2010). The significance of (anti-)clustering (or deviation from a Poissonian process) can be assessed by comparing the empirical $p(\boldsymbol{R})$ to that built upon the sample of data randomly distributed in time (i.e., following Poisson process) with the same number of events as the empirical catalog (Davidsen et al., 2017, 2021). To strengthen the inference, one can further condition $p(\boldsymbol{R})$ on the magnitude of events (i.e., larger events are expected to trigger more frequently), or on the difference in magnitudes of adjacent events (i.e., larger events preceding the smaller ones signify aftershock sequences). Such conditioning of the data set should amplify any potential triggering behavior if it exists.

2.4.6. Focal Mechanisms

For 14 earthquakes we calculated double-couple (DC) constrained moment tensors (MTs) using the hybridMT moment tensor inversion package (Kwiatek et al., 2016) and time integrals of the first P-wave ground displacement pulses including sign information (e.g., Amemoutou et al., 2021) calculated from integrated velocity seismogram. For each event, we performed 200 realizations of the moment tensor by perturbing input station take-off angles (by up to $\pm 6°$ to simulate the uncertainties in the velocity model and location, see Martínez-Garzón et al., 2017) and input P-wave amplitudes (by up to 30% to simulate effects of noise, see Davi et al., 2013; Stierle et al., 2014). This sampling procedure aimed to identify stable focal mechanisms that are insensitive to imposed noise variations and velocity model uncertainties (see also discussion on focal mechanism stability in Leonhardt, Kwiatek, Martinez-Garzon, & Heikkinen, 2021). For each earthquake, the stability of its focal mechanism has been assessed by calculating the 3D rotation angle δ (Kagan, 2007) in-between best solution and 200 sampled solutions (see similar procedure in Goebel et al., 2017; Dresen et al., 2020). We ultimately selected eight moment tensor solutions for which the two standard deviations of δ sampled mechanisms did not exceed 20°. Additionally, we calculated full moment tensors obtaining initially low level of the isotropic components (<10%). However, the performed Bayesian Information Criterion test (Bentz et al., 2018; Cesca et al., 2013) indicated an insignificant improvement of the root-mean-square error between full MT and DC-constrained MT inversion results. Therefore, we decided to use the double-couple constrained moment tensors calculated beforehand.

3. Results

3.1. Seismic Response to Injection Operations

Between January 2020 and the start of the stimulation campaign in May 2020 a total of 197 earthquakes were detected originating in the vicinity of the two wells OTN-2 and OTN-3 at >5.0 km depth. This activity consisted of mostly small seismic events that were likely triggered by engineering operations at the OTN-2 well. A remarkable doublet of well-recorded seismic events with $M_{\mathrm{L}}^{\mathrm{Hel}}$ 1.2 and $M_{\mathrm{L}}^{\mathrm{Hel}}$ 0.6 separated by a few hours occurred

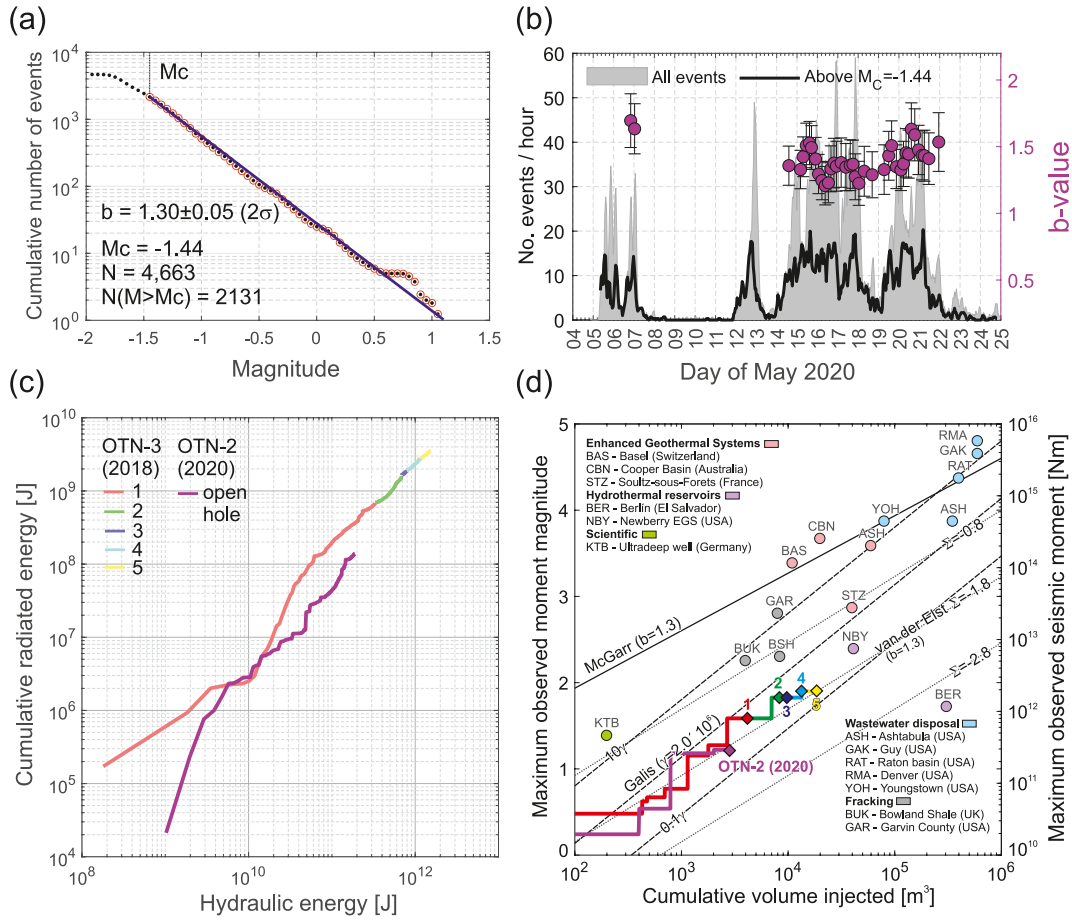

Figure 3. (a): Cumulative frequency-magnitude Gutenberg-Richter distribution calculated for injection phases P2–P4; (b): Temporal evolution of the *b*-value during injection and shortly after injection using a moving window of $N = 250$ events. The vertical error bar corresponds to 2σ error of the b-value estimate; (c): Relation between cumulative hydraulic energy E_H and cumulative seismic radiated energy E_0 during the 2018 and 2020 stimulations; (d): Relation between cumulative fluid volume and maximum earthquake magnitude for the 2018 (color reflect phase 1–5 of injection, see Kwiatek et al., 2019 and Leonhardt et al., 2021; Leonhardt, Kwiatek, Martínez-Garzón, et al., 2021 for details) and 2020 stimulations (magenta).

on 14 April 2020 (Figure 2c). This doublet was preceded by a few smaller events the same day and it was also followed by some activity during the 24 hr following the M_L^{Hel} 0.6 s event. Other than the two main events, event magnitudes of associated activity were $M_L^{\mathrm{Hel}} < -0.5$ (Figure 2c) and they showed no accelerating or decelerating behavior. It is conceivable, that the events were caused by mud replacement operations performed in OTN-2 well. Sparse seismic activity was observed throughout the following 2 weeks with $M_L^{\mathrm{Hel}} < 0.3$, until the beginning of the injection campaign in OTN-2.

The OTN-2 stimulation started on 5 May 2020 and lasted nearly 16 days. Active fluid injection was maintained for half (49%) of the entire time period (Figure 2a). The fluid was injected into the entire OTN-2 open hole section. For technical reasons, the stimulation was separated timewise into four phases (P1–P4 in Figure 2a) (St1 Oy—pers. comm). Each injection phase resulted in a significant increase in seismic moment M_0 and radiated seismic energy release E_0. Similarly to the 2018 stimulation, the E_0 was found to be closely related to the hydraulic energy input E_H (Figure 3c). Hydraulic energy was estimated from:

$$E_H = \int_0^t P(t)\Delta V(t)dt, \tag{6}$$

where P is the average wellhead pressure, ΔV is the injection rate and t is time. We note E_H is estimated at the well head, and as such it is a proxy for the energy change related to fluid injection available in the subsurface

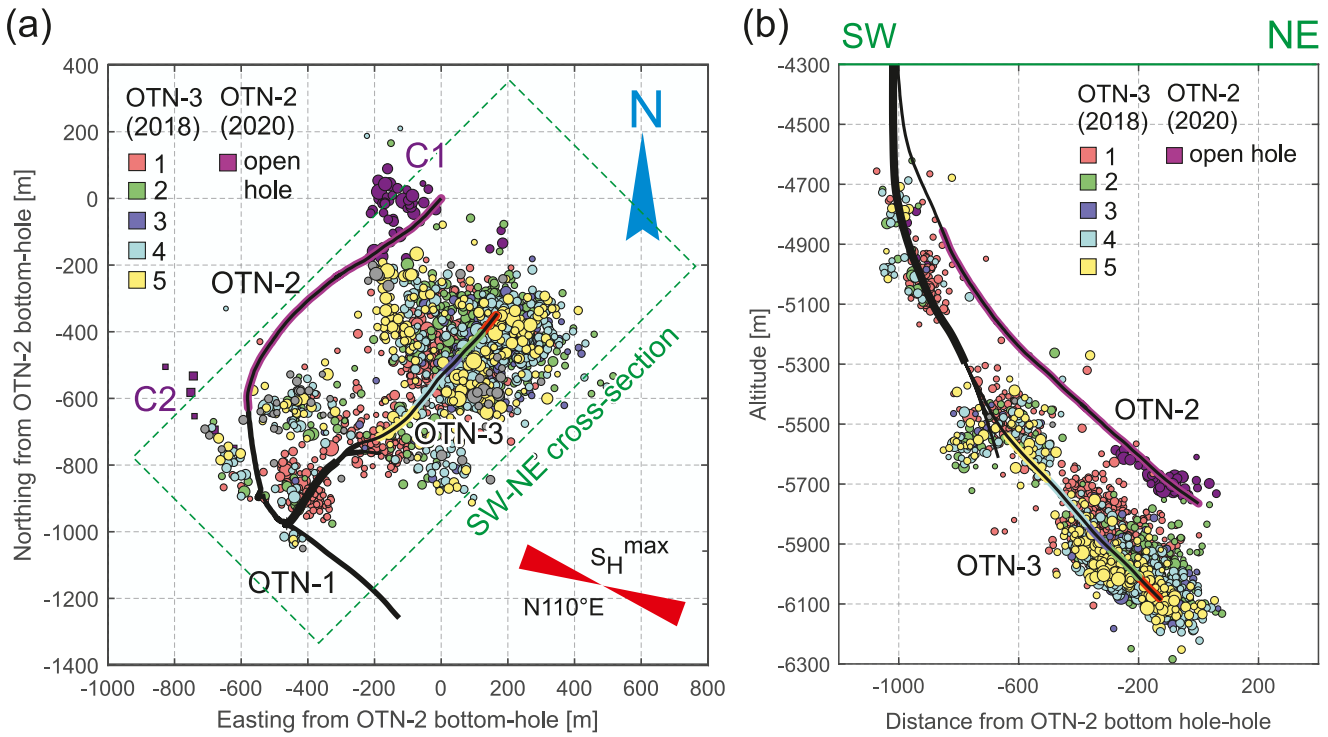

Figure 4. Hypocenters of seismicity from the 2020 stimulation (this study, magenta circles and squares, denoting clusters C1 and C2, respectively) and from past 2018 stimulation (circles color-coded with injection phases 1–5, cf. Leonhardt, Kwiatek, Martínez-Garzón, et al., 2021). (a): Map view; (b): SW-NE-trending depth section along 45° (SW-NE) azimuth. The colored sections of the OTN-3 and OTN-2 wells indicate isolated stimulation intervals (2018) and the open-hole section (2020), respectively. The size of symbols reflects earthquake magnitudes.

(e.g., Maxwell, 2011). We found the cumulative seismic energy release to be proportional to the hydraulic energy (Figure 3c), however, at a slightly lower level of seismic injection efficiency η^{inj} than that observed in 2018.

During the stimulation period a total of 5,427 earthquakes were detected (N = 2,494 with $M_L^{Hel} > M_C = -1.4$) with largest event magnitude $M_L^{Hel} = 1.1$. The evolution of maximum event magnitudes and cumulative seismic moment release roughly followed the trend predicted by the models of Galis et al. (2017) and van der Elst et al. (2016) (Figure 3d). Event magnitudes remained way below values predicted by the model of McGarr (2014). The b-values for the quasi-stationary injection period during injection phases P2–P4, where the injection rates and pressure were relatively stable, is $b = 1.3 \pm 0.1$ at a magnitude of completeness $M_C = -1.4$ (Figure 3a). The observed b-values are similar to those from the 2018 stimulation (b = 1.3, Kwiatek et al., 2019). These b-values are common for induced seismicity (cf. Mignan et al., 2021), but slightly larger than observed for natural earthquakes (b = 1 on average). Similar to the 2018 stimulation in OTN-3 well, at the beginning of stimulation campaign (P1 in Figure 2a) we observe slightly higher b-values, whereas for the remaining period we did not observe statistically significant temporal changes in the b-value (Figure 3b).

Fluid injection ceased on 21 May 2020 with well bleed off (cf. Figure 2a). The seismic monitoring continued during the post-injection phase until 23 Jun 2020 recording 694 earthquakes in total. For the first 4 days of the post-injection period we observed a rapid decline in seismic activity (Figure 2a), followed by a gentler decline of seismic activity (Figure 2d). Small bursts of seismic activity occurred at the end of the monitoring period, likely related to technical operations in the OTN-2 borehole that likely affected the downhole pore fluid pressure. The observed maximum magnitude after shut-in reached M_L^{Hel} 1.0 and occurred 10 days after injection (Figure 2d) stopped.

3.2. Spatiotemporal Evolution of Seismic Events and Focal Mechanisms

The spatial distribution of the seismic activity forms two separate clusters C1 (DD-relocated events) and C2 (absolute locations) shown in Figure 4 as magenta circles and squares, respectively. 42 relocated seismic events

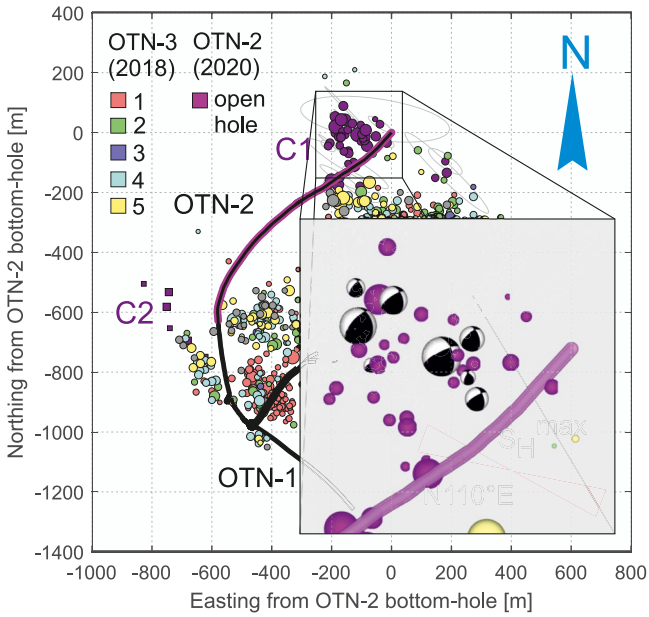

Figure 5. Focal mechanism solutions calculated for the largest earthquakes of the 2020 stimulation using the double-couple constrained moment tensor inversion. The inset shows orthographic view of focal mechanisms from the direction of earth surface (comparable to the upper-hemisphere projection).

observed during the stimulation and after shut-in form a cluster close to the bottom end of the OTN-2 well. The epicentral locations of C1 events extends toward NW similar to the seismicity observed in 2018, but the events are located at a ca. 100–200 m shallower depth (Figure 4b). The C2 cluster is formed by four earthquakes located in the vicinity of the top part of the open-hole section of the OTN-2 well. These events are situated at similar depths as those observed in the uppermost cluster of the 2018 stimulation (cf. Leonhardt, Kwiatek, Martínez-Garzón, et al., 2021), reaching further toward the NW. In contrast to 2018 and irrespective of the small relative relocation uncertainties, we did not observe a spatial migration of seismic events during the 2020 injection, which was likely related to the smaller over-pressures applied compared to 2018. The spatial extension of the clusters C1 and C2 suggest fluid migration toward NW/NNW from the open-hole section with no prominent seismicity detected to the SE of the stimulated OTN-2 well.

The quality-constrained double-couple focal mechanisms display oblique strike-slip/thrust reverse faulting events with one nodal plane aligned in NNW-SSE direction (Figure 5). The obtained mechanisms are similar to those obtained by Rintamäki et al. (2021) for the two largest events from the same stimulation using FOCMEC software and local and regional polarity data (strike/dip/rake = 140°/58°/26°). On average, calculated focal mechanisms are rotated 20° clockwise in fault strike, whereas dip and rake are the same (within the uncertainties obtained by sampling of input data) when compared to focal mechanisms obtained by Rintamäki et al. (2021). The observed rotation is well-explained by a relatively weak control on the strike and rake of mechanisms due to the limited number of stations at larger epicentral distances. However, the obtained mechanisms are in qualitative agreement with a subset of focal mechanism derived by Leonhardt, Kwiatek, Martinez-Garzon, and Heikkinen (2021); Leonhardt, Kwiatek, Martínez-Garzón, et al. (2021) using HASH software (Hardebeck & Shearer, 2002) for the seismicity induced by the 2018 stimulation (Family 2, see Figure 8 in Leonhardt, Kwiatek, Martínez-Garzón, et al. (2021) for details).

3.3. Temporal Catalog Completeness

Any statistical analysis of seismic *b*-value, inter-event time, inter-event time ratio, and magnitude-correlation statistics will depend on the completeness magnitude of the seismic catalog, M_C. As in 2018 (cf. Figure 2 in Kwiatek et al., 2019), the 2020 seismic catalog displays strong daily fluctuations of seismic activity related to anthropogenic surface noises. Due to daily anthropogenic noise fluctuations (cf. Rydelek & Sacks, 1989), the earthquake detection threshold visually follows a sinusoidal pattern increasing by approximately +0.3 and +0.2 during workdays and weekends, respectively (green solid line in Figures 2a and 2b, see Text S2 in Supporting Information S1 for parametric description of the detection threshold curve). Moreover, noise from injection pumps further visibly increased detection level by about +0.3 unit of M_L^{Hel}, masking smaller events (Figure 2b). For best recording conditions (=no injection and during weekend days), the borehole array placed in OTN-3 well could detect earthquakes as small as M_L^{Hel} −1.9 (for signals detected by the borehole array only). Consequently, we found an average magnitude of completeness $M_C = -1.44$ for the seismic catalog covering phases P2–P4 of the 2020 injection (cf. above which the magnitude distribution follows a Gutenberg-Richter power law) (Figure 3a). However, for the statistical analysis related to triggering statistics we used a more conservative magnitude threshold of $M_C^* = -1.25$, which suppressed effects related to short-term catalog incompleteness due to variations in environmental noise levels (cf. dashed orange curve in Figures 2b–2d). Using a lower magnitude threshold for the catalog clearly affects the statistical analysis performed in this study (see Figures S1, S2, and S3 in Supporting Information S1 and discussion below for details).

3.4. Magnitude Correlations

We analyzed the changes in probability $\delta p(\Delta m)$ to observe a magnitude difference $M_{i+1} - M_i < \Delta m$ for events from selected subsets of the earthquake catalog (Figure 6) containing only quasi-stable injection periods avoiding the shut-in phases and resting periods while assuming $M_C^* = -1.25$. The first selected time period

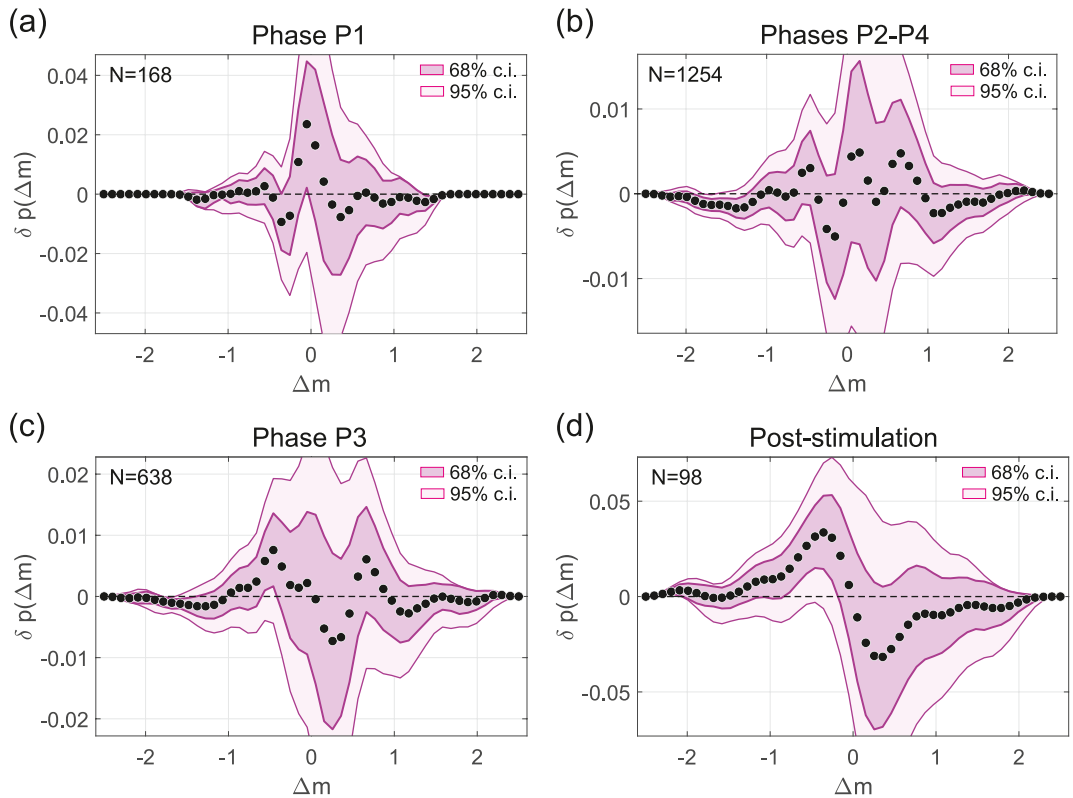

Figure 6. Differences in the probability to observe a magnitude difference $M_{i+1} - M_i < \Delta m$ between selected subset of the catalog containing N earthquakes (black dots) and its randomized versions, which do not exhibit magnitude correlations (Equation 3, light and dark magenta areas correspond to 95% and 68% confidence intervals, respectively). Magnitude correlations correspond to significant deviations from zero. (a): Injection phase P1; (b): Injection phases P2-P4; (c): Injection phase P3; (d): Post-stimulation seismicity (cf. Figure 2 for time intervals).

(Figure 6a) covers the seismicity that occurred during injection phase P1 (from the time when injection rate ramped up to 400 L/s and until ca. 2 hr after the injection shut-in, when the well head pressure dropped below 60 MPa). Here nearly all points of empirical $\delta p(\Delta m)$ fall within 68% confidence lines calculated using multiple resampled distributions of magnitude correlations for which any potential correlations have been destroyed. Moreover, no single point falls outside the 95% confidence interval. This means the selected subset containing phase P1 seismicity does not significantly differ from its randomized version, and thus there is no statistically significant evidence for the existence of event-to-event magnitude correlations in the P1 subset. Accordingly, this also means that short-term local-in-time accelerations or decelerations of seismic energy release are very scarce (if at all present) during injection phase P1. This was also found for magnitude correlations using the entire time period covering phases P2–P4 that include short resting periods in between phases (Figure 6b) as well as when one considers the individual phases such as P3 alone (Figure 6c). This is a clear indication of the absence of correlations between magnitudes. Finally, the post-stimulation catalog (Figure 6d) indicates, as intuitively expected, some signatures of weak correlations between magnitudes, which manifest themselves as a substantial deviation of $\delta p(\Delta m)$ from zero baseline around $\Delta m = 0$. In particular, these deviations indicate that subsequent events of similar magnitude are less likely to occur as expected by random chance such that there is a tendency that larger and smaller events alternate. However, these weak magnitude correlations are not significant at the 95% confidence level and the number of events is very small ($N = 98$). Lowering the magnitude of completeness below the conservative threshold of $M_C^* = -1.25$ weakens the reliability of inferring magnitude correlations (Figure S1 in Supporting Information S1). Specifically, short-period catalog incompleteness manifests itself in a higher likelihood of subsequent events of similar magnitude. This systematic bias can be clearly seen, for example, in Figure S1a–S1b in Supporting Information S1 leading to deviations beyond the 95% confidence level.

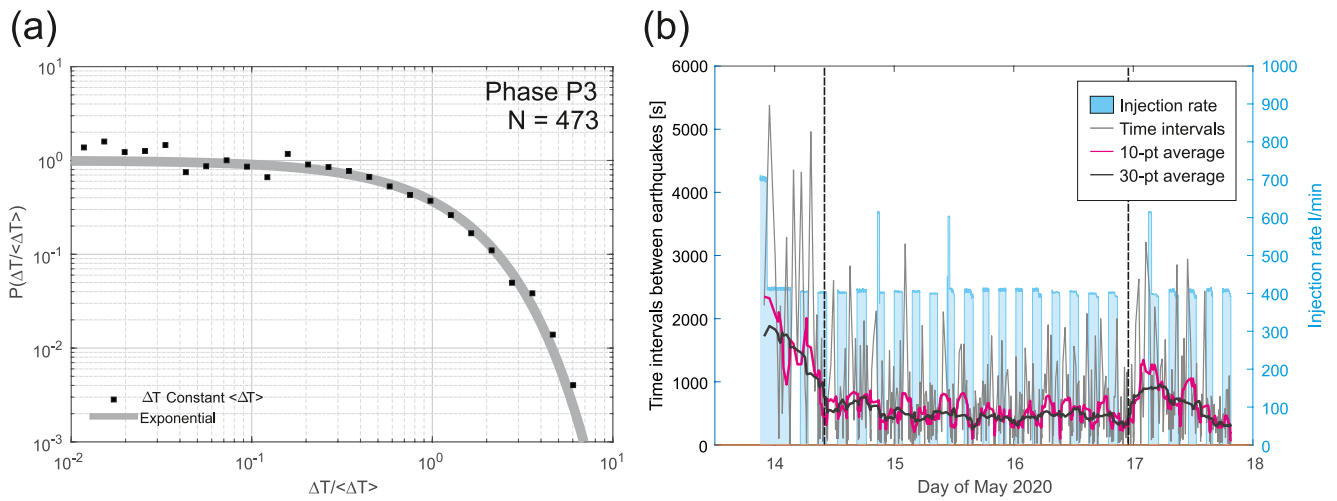

Figure 7. (a): Empirical distribution of interevent times (black squares) and an exponential with the same mean (solid gray line) for selected time interval of seismicity from phase P3 of injection ($M > M_C^*$). (b): Interevent-times of seismic events from phase P3 of injection (gray line) with 10-and 30-points moving average (cyan and black line, respectively). To calculate empirical distribution in (a), the quasi-stable time interval between two dashed vertical lines was used.

3.5. Temporal Clustering Properties

The empirical PDF of inter-event times, $p(\Delta T/\langle\Delta T\rangle)$ is shown in Figure 7a for injection phase P3 containing sufficient number of events above M_C^* thus allowing for reliable estimations. We selected a narrower time period bounded by dashed lines in Figure 7b which is characterized by a long-lasting and quasi-stable injection without any major interruption but with repeating pressurization episodes (cf. Figure 2) of similar amplitude, leading to quasi stable seismicity rates. This allowed us to use a scalar $\langle\Delta T\rangle$ value to normalize the interevent time distribution $p(\Delta T/\langle\Delta T\rangle)$, allowing a comparison with other case studies. We compared the empirical distribution (circles in Figure 7a) to an exponential distribution with the same mean of 1 (solid line in Figure 7a). A Kolmogorov-Smirnov test could not reject the hypothesis that the data are consistent with this exponential distribution at high confidence ($p = 0.61$). Since the exponential distribution is the probability distribution of the inter-event times of a Poisson process, where events occur independently at a constant average rate, our findings strongly suggests that the seismicity, when not affected by changing injection, follows a Poissonian process.

This is further confirmed by panels (a–d) of Figure 8 showing the empirical PDFs of inter-event time ratios, $p(\boldsymbol{R})$, calculated for selected subsets of the seismic catalog during (Figures 8a–8c) and after stimulation (Figure 8d). We assumed a conservative magnitude of completeness $M > M_C^*$. It is clearly seen that for the selected catalog, the inter-event time ratios fall within a 95% confidence interval of a (non-homogeneous) Poisson process with the same number of events. This means that these subsets are unlikely to contain any signatures of immediate temporal clustering (acceleration) or anti-clustering (deceleration) of seismic activity. Interestingly, this holds for the post-stimulation activity as well (Figure 8d) where the stress relaxation effects are expected. For comparison, $p(\boldsymbol{R})$ calculated for the aftershock sequence of a M_W 1.9 event recorded in the Mponeng deep gold mine (Kwiatek et al., 2010, 2011) and from the Alpine fault system (cf. Michailos, 2019; Michailos et al., 2019) are shown in Figures 8e and 8f. The sequences contain overlapping background seismicity and aftershocks. Theses sequences display clear indications for local temporal clustering of seismicity, as evidenced by strong deviations of empirical $p(\boldsymbol{R})$ which exceed the confidence intervals at the edges. We further constrained the input inter-event time vectors $\boldsymbol{R}$ and calculated conditional probabilities $p(\boldsymbol{R}|M > -0.8)$ and $p(\boldsymbol{R}|\Delta M < 0)$. The conditioning should emphasize any potential (anti-)clustering behavior because larger events are expected to trigger subsequent events more frequently and also larger events preceding smaller ones promote aftershock sequences that favor triggering. The obtained results suggest the conditioned catalog subsets either do not display significant (anti-)clustering properties (Figures S2 and S3 in Supporting Information S1).

4. Discussion

The analysis of seismic activity induced by the May 2020 stimulation campaign performed in OTN-2 well within the Helsinki St1 EGS project shows a similar trend as already observed during 2018 OTN-3 well stimulation.

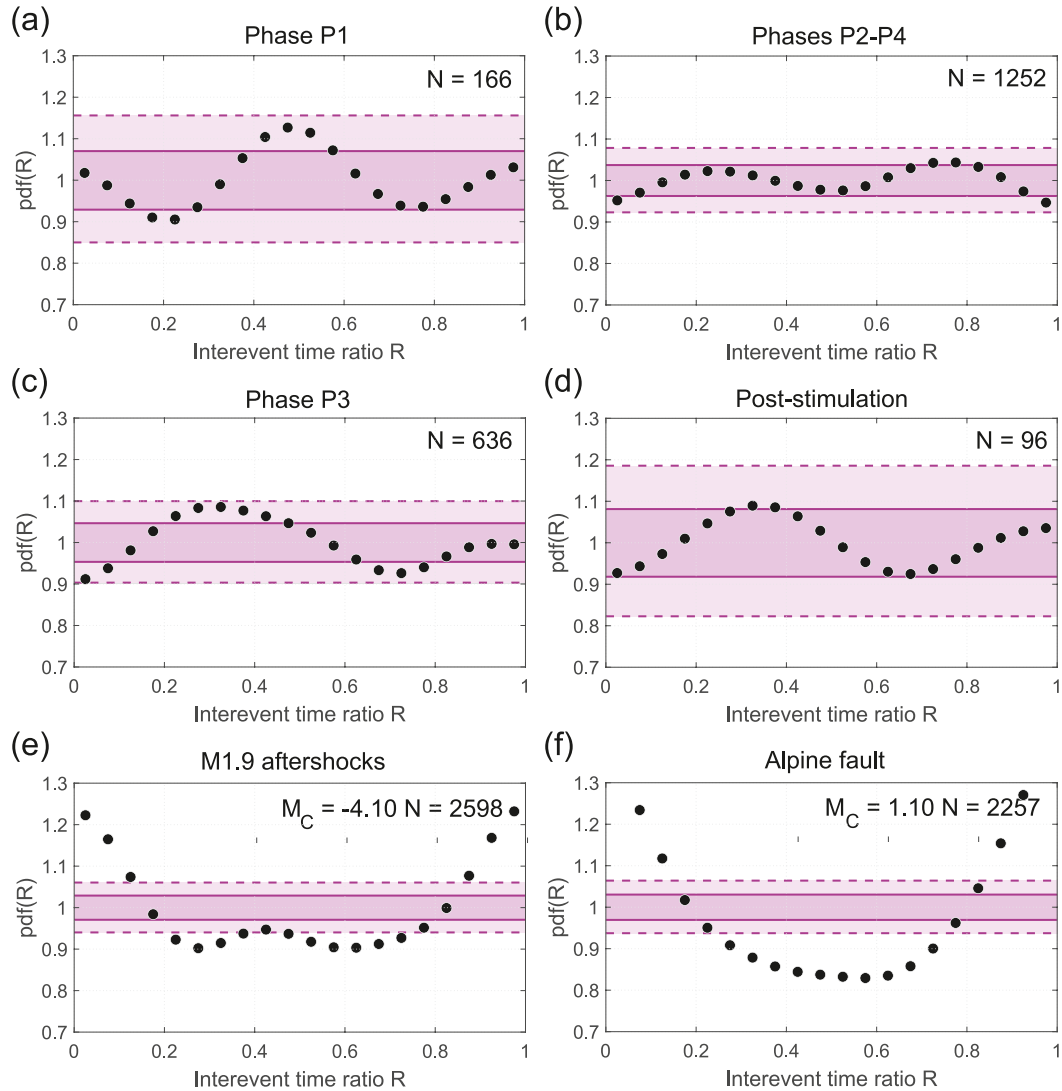

Figure 8. Probability density function of interevent time ratios, $p(\mathbf{R})$, for seismicity from different phases of 2020 stimulation and above the conservative magnitude of completeness, $M_C^* = -1.25$. (a): Phase P1; (b) Phase P2–P4; (c): Phase P3; (d) Post-stimulation. For comparison, (e): Aftershock sequence of M_W 1.9 earthquake recorded in Mponeng deep gold mine (Kwiatek et al., 2010, 2011); (f): Alpine fault catalog containing background activity and aftershock sequences (Michailos, 2019; Michailos et al., 2019) are shown (see text for discussion). Solid and dashed magenta lines correspond to 68% and 95% confidence intervals of $p(\boldsymbol{R})$ expected from events randomly distributed in time, assuming same number of events as in the particular catalog subset.

Our results confirm a *stable* evolution of induced earthquake activity during a pressure-controlled fluid-injection. Following Bentz et al. (2020) we define a *stable* evolution of seismicity by low and time-invariant seismic injection efficiency η^{inj} during injection operations, with a maximum magnitude evolution related to injected fluid volume (c.f. Galis et al., 2017; McGarr, 2014; Shapiro et al., 2010; van der Elst et al., 2016). For a *stable* seismicity evolution, the maximum magnitude is bound by the elastic strain energy stored by fluid injection in a geothermal system (Galis et al., 2017). This is in clear contrast to an *unstable* seismicity evolution, where seismic injection efficiency is observed to be either high or continuously increasing such as in the Pohang EGS project (Bentz et al., 2020). We posit that temporal increase in η^{inj}may indicate a pending transition from *stable* conditions with arrestable seismic events to *unstable or run-away* conditions (Galis et al., 2017). Run-away ruptures are driven by tectonic stresses and cannot be controlled by engineering operations. Maximum magnitudes of events are related to the size of faults in the stimulated volume.

Stable, pressure-controlled seismic response to fluid injection in geothermal reservoirs will largely depend on the absence of critically stressed large faults within or near the stimulated rock volume, (Ellsworth et al., 2019; McGarr, 2014). Activation and growth of a small-scale network of randomly distributed fractures and joints may be less prone to host larger seismic events (cf. discussion in Martínez-Garzón et al., 2020). Therefore, near-real-time assessment of spatio-temporal behavior of seismic event locations, focal mechanisms, and temporal evolution of statistical properties such as *b*-value, c-value, and d-value (Dresen et al., 2020; Eaton & Igonin, 2018; Goebel et al., 2017; Schoenball et al., 2015) is key to identify the existence/emergence of large fault structures.

In addition to the fault inventory and geometry, the stress state of reservoir faults is important for potential significant stress transfer via earthquake-earthquake interactions (Kwiatek et al., 2019). Fault stress state, static, and dynamic stress transfer, to name a few, are known to affect the evolution of seismic activity in a geothermal system (e.g., Martínez-Garzón et al., 2018; Schoenball et al., 2012; Shen et al., 2021). There is general consensus that mitigation actions must be applied when stress transfer from earthquakes generates significant stress changes driving seismicity even without fluid injection. However, mitigations may be ineffective to reduce the seismic hazard (Brown & Ge, 2018).

In this study we calculated diagnostic statistical seismic parameters that assist I discriminating a pressure-controlled stable injection phase from a stimulated reservoir response dominantly controlled by tectonics. In particular, we propose that the stability of (and preferably absence) of earthquake triggering processes is an important characteristic of stable reservoirs. We show that earthquake interaction processes may be described using simple statistical parameters obtainable in near-realtime from the growing seismic catalog. Such information is complementary to information on seismic efficiency η_{inj} evolution and information on the structural complexity, and, combined with other parameters such as b-value evolution (e.g., Gulia & Wiemer, 2019) may help to detect the evolution of seismicity toward unstable, runaway state.

The seismicity induced so far by two stimulation campaigns in the Helsinki geothermal project present well-constrained examples of *stable* induced seismicity passively responding to injection operations. Both stimulation campaigns share common features including comparable and generally time-invariant seismic injection efficiencies and *b*-values (Figures 3a and 3b). Following Main (1991), stationary *b*-values indicate a *stable* damage evolution. This is supposed to reflect evolution and growth of a distributed fracture network as derived from locations and focal mechanisms in contrast to progressive coalescence of fractures toward system-wide runaway failure. For both stimulations no notable time delays existed between start of pumping and seismicity during the entire stimulation. Seismicity always occurred in spatially-broad zones once ca. 70 MPa well-head pressure was exceeded. This excludes Kaiser effect (Baisch et al., 2002; Kaiser, 1953), where seismicity occurred only after exceeding the past values of well head pressure or injection rate (see field example from e.g., Kwiatek et al., 2014), suggesting that a distributed network of fractures re-activates beyond a critical well-head pressure during stimulation. The observed invariance of *b*-values may also indicate limited overall stress buildup in the reservoir due to fluid injection (Scholz, 1968; Schorlemmer et al., 2005), with injection-induced stresses being distributed in a 3D-volume of distributed fractures rather than on a single major structure. Observations of *b*-values are in contrast to data from Basel, Switzerland or Pohang, South Korea (Bachmann et al., 2012; Ellsworth et al., 2019) where decreasing *b*-values were observed toward the occurrence of larger run-away earthquakes on a major fault.

Evolution of maximum event magnitudes during the 2020 and 2018 stimulations follows a trend predicted by Galis et al. (2017) or van der Elst et al. (2016) who stated that expected upper limit to the maximum magnitudes for the stable, pressure-controlled seismicity is proportional to the total fluid volume $V^{3/2}$. Following the Galis et al. (2017) study, the observed trend suggests that the maximum event magnitude is related to the amount of elastic energy stored in the reservoir due to fluid injection. Lab experiments and field observations suggest that energy dissipation involves significant contribution from aseismic (here interpreted as out-of-the-seismic band, cf. Dresen et al., 2020) deformation (McGarr & Barbour, 2018). However, the existing models relating seismic moment evolution and maximum magnitude of events to the injected total fluid volume do not capture the effect of injection rate on seismicity and aseismic deformation. Flow rate and the rate of pore fluid pressure build-up are expected to affect induced seismic activity, as was observed from waste water injection in Oklahoma (Weingarten et al., 2015), laboratory tests (Passelègue et al., 2018; Wang, Kwiatek, Rybacki, Bonnelye, et al., 2020) and numerical modeling (Almakari et al., 2019; Rudnicki & Zhan, 2020). This highlights the importance of hydraulic energy input rate as the actual parameter controlling maximum magnitude and seismic hazard

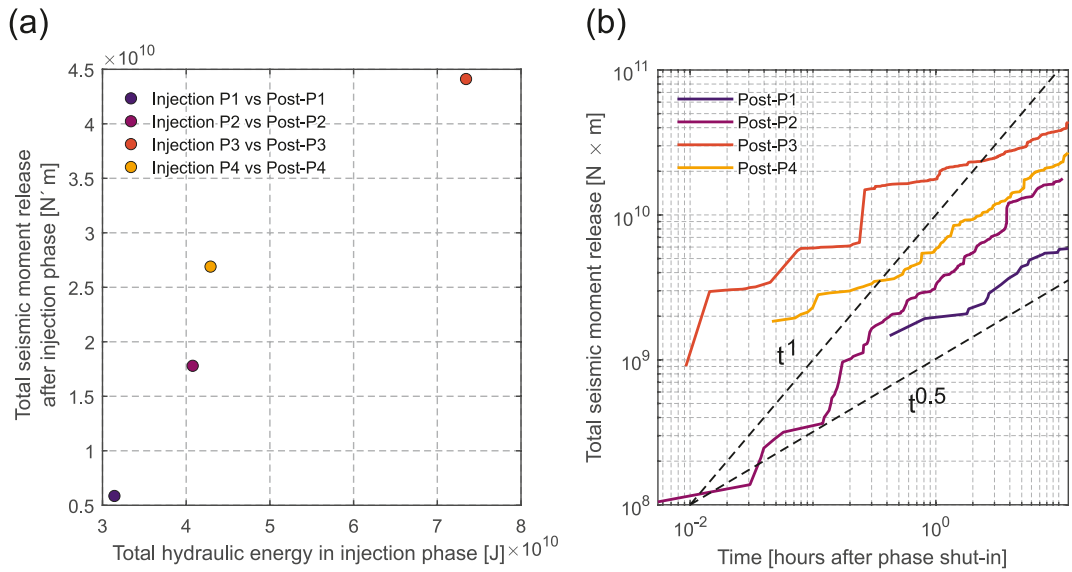

Figure 9. (a) Relation between total hydraulic energy of injection phase P1–P4 and total seismic moment releases within 12-hr time period following the injection phase. (b) Seismic moment release evolution within 12 hr following injection phases P1–P4.

during stable phases of injection operations. For time invariant *b*-values, seismic hazard is related solely to seismicity rate changes. Wang, Kwiatek, Rybacki, Bonnelye, et al. (2020) showed that the mechanical response (slip rate/moment rate) of a single planar fault, as well as the associated small-scale acoustic emission activity (moment rate) may vary significantly with respect to pressurization rate (~hydraulic energy rate). With increasing pore fluid pressurization rate, seismic moment release changed from stable and almost linear behavior to short "run-away" slip at high pressurizations rates. During the 2020 Helsinki OTN-2 well stimulation, we did not observe a non-linear increase of seismic energy release in response to hydraulic energy input. This was evidenced by a stable seismic injection efficiency, likely favored by very low injection pressures applied. Only during a relatively short period when high hydraulic energy input rates were applied during the 2018 Helsinki OTN-3 well stimulation, we observed a clear acceleration of seismic energy release leading to progressive increase of seismic injection efficiency (cf. Kwiatek et al., 2019 for details). However, with immediate mitigation procedures applied in response to the occurrence of large magnitude events (Ader et al., 2019), seismic injection efficiency could be stabilized again. In summary, both stimulation campaigns in 2018 and 2020 represent pressure-controlled, *stable* induced seismicity where seismic/aseismic energy dissipation is clearly related to hydraulic energy input. This points toward a limited possibility for runaway ruptures to occur in a tectonic environment without significant structural inhomogeneity. However, we note our observations do not allow predicting the extent of *stable* seismicity behavior with further fluid injection limited by a maximum arrestable event magnitude (Galis et al., 2017).

In many geothermal systems induced seismicity continues beyond shut-in. At the Basel Deep Heat Mining HDR site seismicity following the stimulation campaign in 2006 is still ongoing after 15 years. In Helsinki, the occurrence of a relatively large earthquake of magnitude $M_{\mathrm{L}}^{\mathrm{Hel}} = 1.2$ in April 2020 before the 2020 stimulation campaign in OTN-2 was unexpected. Within the framework described in previous paragraph, the occurrence of this event, as well as the associated seismicity in preceding months could be related to the relaxation of the elastic strain energy accumulated in the reservoir during the 2018 stimulation. However, some natural earthquakes ($M_{\mathrm{W}}1.7$ and $M_{\mathrm{W}}1.4$, see Kwiatek et al., 2019 for details) did occur at epicentral distances not exceeding a few km from the project site in 2011. Thus it is difficult to attribute any event within this time period to being natural or triggered/induced without detailed information on engineering operations performed at the site.

For the 2018 and 2020 stimulation campaigns, we found seismic activity to quickly decline within 24hr following each shut-in (Figures 2a and 2d). This supports our contention that the observed seismicity during the stimulations was entirely due to a local stress perturbation induced by injection. Interestingly, we found that the cumulative seismic energy release within 12 hr after phases P1-P4 of the 2020 injection scales well with the total hydraulic energy accumulated during the preceding injection phase (Figure 9a). In addition, the rate of seismic moment decrease during shut-in phases is similar for between 24-hr periods following phases P1–P4, scaling as

$\sum M_0(t) \propto t^{\alpha}$, where t is the time since the begin of shut-in (Figure 9b) and α between 0.5 and 1.0 (dashed lines in Figure 9b). The decrease of seismic moment rate is reflecting the seismicity rate changes in a form of Omori (Utsu, 1961) type behavior (see examples in Figure S5 of Supporting Information S1). However, the rate decay occurs without associated temporal changes in the b-value that are sometimes reported for aftershock sequences (e.g., Gulia & Wiemer, 2019).

The observed seismic response clearly relates to the reservoir structure. There is no evidence for activation of a larger fault that was previously unknown within the reservoir or its immediate surrounding. Relocated events (location error ±41 m in horizontal direction) of cluster C1 (Figure 4) suggest extension of a broad damage zone already observed during 2018 OTN-3 stimulation further to the NW. Focal mechanisms calculated using moment tensor inversion display one nodal plane in good agreement with the regional stress field (cf. Leonhardt, Kwiatek, Martinez-Garzon, & Heikkinen, 2021; Leonhardt, Kwiatek, Martínez-Garzón, et al., 2021), suggesting that the stimulation reactivated a spatially-broad network of fractures trending mostly NW-NNW, but at shallower depth than observed in 2018 (cf. Figure 5).

Kwiatek et al. (2019) found that >85% of seismic events induced by the 2018 stimulation displayed properties of background seismicity. The events followed a quasi-stationary Poissonian process with earthquakes randomly distributed over the stimulated volume and in time. A spatio-temporal analysis could not be performed for the 2020 seismicity catalog due to a limited number of seismic events. Instead, we employed a number of simple statistical measures of clustering in the time domain, all confirming very limited interaction between earthquakes from the 2020 seismic catalog. The empirical distribution of inter-event times of seismicity from Phase P3 of the injection campaign conform to an exponential distribution. This indicates that earthquakes occur randomly in time, when we properly select the catalog accounting for changing seismicity rates due to variation in the injection rates and for temporal variabilities of . Indeed, the statistical analysis of inter-event time ratios revealed no temporal clustering and anticlustering between earthquakes occurring during and after the stimulation campaign (Figures 8a–8d). The empirical distributions were statistically indistinguishable from (non-homogeneous) Poissonian-distributed seismicity as clearly shown for isolated injection phases P1 and P3 (Figures 8a and 8c). Even the subset of the catalog covering phases P2–P4 (Figure 8b) that includes resting periods, as well as the post-injection catalog (Figure 8d) do not show any signatures of temporal (anti-)clustering. This is also the case when we further condition the catalog subsets trying to emphasize the potential (anti-)clustering behaviors (Figures S2 and S3 in Supporting Information S1). We therefore conclude that earthquakes forming the catalog occur randomly in time following a (non-homogeneous) Poissonian process (cf. Broccardo et al., 2017; Mignan et al., 2017). The variations in seismicity rate are modulated by the hydraulic energy input rate, as expected for induced seismicity (Goebel et al., 2019; Langenbruch et al., 2011), but show no temporal clustering—in contrast to other fluid-driven settings (Karimi & Davidsen, 2021; Maghsoudi et al., 2018) as well as laboratory experiments and natural earthquakes (e.g., Davidsen & Kwiatek, 2013; Davidsen et al., 2021, and references therein). Neither the enhanced stressing rates due to fluid injection nor stress relaxation after the stimulation phases, nor the localization of seismicity within confined zones caused triggering.

Frequently, a prominent structure such as a fault, which causes local stress concentration, results in earthquake triggering (Davidsen et al., 2017, 2021). However, no major fault was reported for the stimulated reservoir, which may explain the lack of triggering in agreement with Schoenball et al. (2012) for Soultz-sous-Forets/France geothermal site and Martínez-Garzón et al. (2018) for The Geysers geothermal field in California.

Magnitude correlations are insignificant for 95% confidence intervals in all analyzed cases. These include subsets of the catalog covering selected stimulation phases (Figures 6a–6c) and the post-stimulation catalog (Figure 6d). Probability differences $\delta p(\Delta m)$ do not deviate significantly from zero considering confidence intervals. This indicates a lack of local-in-time accelerations or decelerations of seismic energy release in the catalog, in agreement to studies of induced nano- and picoseismicity (Davidsen et al., 2012). The observed lack of magnitude correlations supports the assumption of independent earthquake magnitudes and applying probabilistic methods of seismic hazard assessment for the stimulation site (Ader et al., 2019). The lack of statistically significant magnitude correlations also argues against existence of any cascade-type nucleation processes (e.g., Ellsworth & Beroza, 1995; McLaskey, 2019). Cascade processes rests on some form of stress transfer between earthquakes, for which we find no statistical evidence down to our conservative magnitude of completeness of $M_C^* = -1.25$, that is, faults/fracture sizes of the order of a few meters. Similar to what has been found for previous statistical

properties, magnitude correlations are also sensitive to variations in completeness level caused by injection- and day/night cycle-related changes in earthquakes detectability.

5. Conclusions

Two hydraulic stimulation campaigns performed in 2018 and 2020 in two different wells in the Helsinki suburban area as part of the St1 Deep Heat project each resulted a stable evolution of induced seismic activity that could be controlled by adjusting the injection operations (cf. Kwiatek et al., 2019). We posit that the pressure-controlled seismicity evolved in response to an adaptive injection strategy balancing the hydraulic energy input with seismic energy release output and favored by reservoir structures and stress state. In an effort to identify proxies characterizing seismicity evolution as either stable or run-away we analyzed a series of seismic parameters signifying potential interaction between the earthquakes. We found that the absence of earthquake—earthquake triggering is an important indicator for a stable injection. Using the proposed simple diagnostic measures of interactions in near-real-time monitoring may allow to detect potential deviations from a stable state, potentially indicating increasing seismic hazard. We summarize the characteristics of stable reservoir as observed in the 2018 and 2020 stimulations as follows:

1. The seismicity down to at least magnitude −1.25 (source sizes of a couple of m) passively responded to injection operations. It displays representative properties of background seismicity that can be well described by a non-stationary Poisson process and is modulated by the hydraulic energy input rate. Although the seismicity tends to cluster in space and time in response to fluid injection, no interaction between earthquakes is observed despite highly varying hydraulic energy input rates.
2. Seismic energy output rate, without significant temporal variations in b-value indicating activation of a stationary and spatially-distributed fracture network, is proportional to the hydraulic energy input rate. The ratio of seismic to hydraulic energy is not changing over time substantially.
3. The maximum magnitude in both 2018 and 2020 stimulations is bound by the current level of elastic strain energy stored in the geothermal system due to injection, through total hydraulic energy input and input rate.
4. The relocated seismic data, their relative precision in comparison to total spatial extent of the seismicity clearly suggest (re)activation of the volume of distributed and likely subparallel fractures. The limited magnitudes of seismic events and low event density in the stimulated reservoir volume inhibit triggering. Instead, fluid injection caused largely aseismic deformation, that is, brittle processes not capture by the seismic band of the monitoring system.
5. The response of the induced reservoir seismicity to the injection operations supports the use of deterministic models and classical probabilistic methodologies for seismic hazard assessment at this geothermal project.

Data Availability Statement

Catalog of detections, located and relocated events and focal mechanisms is available as separate data publication: Kwiatek et al. (2022), https://doi.org/10.5880/GFZ.4.2.2022.001.

Acknowledgments
The authors would like to thank M. Uski, T. Vuorinen, K. Oinonen, J. Kortstrom, B. Orlecka-Sikora, and S. Lasocki for useful discussions during preparation of the manuscript. The authors thank A. Mignan, D. Schmitt, and an anonymous reviewer for their helpful comments. P.M.G. acknowledges funding from the Helmholtz Association in the frame of the Young Investigators Group VH-NG-1232 (SAIDAN). Open Access funding enabled and organized by Projekt DEAL.

References

Ader, T., Chendorain, M., Free, M., Saarno, T., Heikkinen, P., Malin, P. E., et al. (2019). Design and implementation of a traffic light system for deep geothermal well stimulation in Finland. *Journal of Seismology*, *24*(5), 991–1014. https://doi.org/10.1007/S3950-019-09853-y

Alghannam, M., & Juanes, R. (2020). Understanding rate effects in injection-induced earthquakes. *Nature Communications*, *11*(1), 3053. https://doi.org/10.1038/s41467-020-16860-y

Almakari, M., Dublanchet, P., Chauris, H., & Pellet, F. (2019). Effect of the injection scenario on the rate and magnitude content of injection-induced seismicity: Case of a heterogeneous fault. *Journal of Geophysical Research: Solid Earth*, *124*, 8426–8448. https://doi.org/10.1029/2019JB017898

Amemoutou, A., Martínez-Garzón, P., Kwiatek, G., Rubinstein, J. L., & Bohnhoff, M. (2021). Earthquake source mechanisms and stress field variations associated with wastewater-induced seismicity in Southern Kansas, USA. *Journal of Geophysical Research: Solid Earth*, *126*, e2020JB021625. https://doi.org/10.1029/2020JB021625

Bachmann, C. E., Wiemer, S., Goertz-Allmann, B. P., & Woessner, J. (2012). Influence of pore-pressure on the event-size distribution of induced earthquakes. *Geophysical Research Letters*, *39*(9), L09302. https://doi.org/10.1029/2012GL051480

Baisch, S. (2020). Inferring in situ hydraulic pressure from induced seismicity observations: An application to the cooper basin (Australia) geothermal reservoir. *Journal of Geophysical Research: Solid Earth*, *125*, e2019JB019070. https://doi.org/10.1029/2019jb019070

Baisch, S., Bohnhoff, M., Ceranna, L., Tu, Y., & Harjes, H.-P. (2002). Probing the crust to 9-km depth: Fluid injection experiments and induced seismicity at the KTB superdeep drilling hole, Germany. *Bulletin of the Seismological Society of America*, *92*(6), 2369–2380. https://doi.org/10.1785/0120010236

Bentz, S., Kwiatek, G., Martínez-Garzón, P., Bohnhoff, M., & Dresen, G. (2020). Seismic moment evolution during hydraulic stimulations. *Geophysical Research Letters*, *47*(5), e2019GL086185. https://doi.org/10.1029/2019GL086185

Bentz, S., Martínez-Garzón, P., Kwiatek, G., Bohnhoff, M., & Renner, J. (2018). Sensitivity of full moment tensors to data preprocessing and inversion parameters: A case study from the Salton Sea Geothermal Field. *Bulletin of the Seismological Society of America*, *108*(2), 588–603. https://doi.org/10.1785/0120170203

Broccardo, M., Mignan, A., Wiemer, S., Stojadinovic, B., & Giardini, D. (2017). Hierarchical Bayesian modelling of fluid-induced seismicity. *Geophysical Research Letters*, *44*(22), 11357–11367. https://doi.org/10.1002/2017GL075251

Brown, M. R. M., & Ge, S. (2018). Small earthquakes matter in injection-induced seismicity. *Geophysical Research Letters*, *45*, 5445–5453. https://doi.org/10.1029/2018gl077472

Catalli, F., Meier, M.-A., & Wiemer, S. (2013). The role of Coulomb stress changes for injection-induced seismicity: The Basel enhanced geothermal system. *Geophysical Research Letters*, *40*(1), 72–77. https://doi.org/10.1029/2012GL054147

Catalli, F., Rinaldi, A. P., Gischig, V., Nespoli, M., & Wiemer, S. (2016). The importance of earthquake interactions for injection-induced seismicity: Retrospective modelling of the Basel Enhanced Geothermal System. *Geophysical Research Letters*, *43*(10), 4992–4999. https://doi.org/10.1002/2016GL068932

Cesca, S., Rohr, A., & Dahm, T. (2013). Discrimination of induced seismicity by full moment tensor inversion and decomposition. *Journal of Seismology*, *17*(1), 147–163. https://doi.org/10.1007/S3950-012-9305-8

Cochran, E. S., Wickham-Piotrowski, A., Kemna, K. B., Harrington, R. M., Dougherty, S. L., & Peña Castro, A. F. (2020). Minimal clustering of injection-induced earthquakes observed with a large-n seismic array. *Bulletin of the Seismological Society of America*, *110*(5), 2005–2017. https://doi.org/10.1785/0120200101

Davi, R., Vavryčuk, V., Charalampidou, E.-M., & Kwiatek, G. (2013). Network sensor calibration for retrieving accurate moment tensors of acoustic emissions. *International Journal of Rock Mechanics and Mining Sciences*, *62*, 59–67. https://doi.org/10.1016/j.ijrmms.2013.04.004

Davidsen, J., Goebel, T., Kwiatek, G., Stanchits, S., Baró, J., & Dresen, G. (2021). What controls the presence and characteristics of aftershocks in rock fracture in the lab? *Journal of Geophysical Research: Solid Earth*, *126*(10), e2021JB022539. https://doi.org/10.1029/2021JB022539

Davidsen, J., & Green, A. (2011). Are earthquake magnitudes clustered? *Physical Review Letters*, *106*(10), 108502. https://doi.org/10.1103/PhysRevLett.106.108502

Davidsen, J., & Kwiatek, G. (2013). Earthquake interevent time distribution for induced micro-nano- and picoseismicity. *Physical Review Letters*, *110*(6), 068501. https://doi.org/10.1103/PhysRevLett.110.068501

Davidsen, J., Kwiatek, G., Charalampidou, E.-M., Goebel, T. H. W., Stanchits, S., Rueck, M., & Dresen, G. (2017). Triggering processes in rock fracture. *Physical Review Letters*, *119*(6), 068501. https://doi.org/10.1103/PhysRevLett.119.068501

Davidsen, J., Kwiatek, G., & Dresen, G. (2012). No evidence of magnitude clustering in an aftershock sequence of nano- and picoseismicity. *Physical Review Letters*, *108*(3), 038501. https://doi.org/10.1103/PhysRevLett.108.038501

Dresen, G., Kwiatek, G., Goebel, T., & Ben-Zion, Y. (2020). Seismic and aseismic preparatory processes before large stick–slip failure. *Pure and Applied Geophysics*, *177*(12), 5741–5760. https://doi.org/10.1007/s00024-020-02605-x

Eaton, D. W., & Igonin, N. (2018). What controls the maximum magnitude of injection-induced earthquakes? *The Leading Edge*, *37*(2), 135–140. https://doi.org/10.1190/tle37020135.1

Ellsworth, W. L., & Beroza, G. C. (1995). Seismic evidence for an earthquake nucleation phase. *Science*, *268*(5212), 851–855. https://doi.org/10.1126/science.268.5212.851

Ellsworth, W. L., Giardini, D., Townend, J., Ge, S., & Shimamoto, T. (2019). Triggering of the Pohang, Korea, earthquake (Mw 5.5) by Enhanced Geothermal System Stimulation. *Seismological Research Letters*, *90*(5), 1844–1858. https://doi.org/10.1785/0220190102

Font, Y., Kao, H., Lallemand, S., Liu, C.-S., & Chiao, L.-Y. (2004). Hypocentre determination offshore of eastern Taiwan using the maximum intersection method. *Geophysical Journal International*, *158*(2), 655–675. https://doi.org/10.1111/j.1365-246X.2004.02317.x

Galis, M., Ampuero, J. P., Mai, P. M., & Cappa, F. (2017). Induced seismicity provides insight into why earthquake ruptures stop. *Science Advances*, *3*(12), eaap7528. https://doi.org/10.1126/sciadv.aap7528

Giardini, D. (2009). Geothermal quake risks must be faced. *Nature*, *462*(7275), 848–849. https://doi.org/10.1038/462848a

Gischig, V. S., & Wiemer, S. (2013). A stochastic model for induced seismicity based on non-linear pressure diffusion and irreversible permeability enhancement. *Geophysical Journal International*, *194*(2), 1229–1249. https://doi.org/10.1093/gji/ggt164

Goebel, T. H. W., Kwiatek, G., Becker, T. W., Brodsky, E. E., & Dresen, G. (2017). What allows seismic events to grow big?: Insights from b-value and fault roughness analysis in laboratory stick-slip experiments. *Geology*, *45*(9), 815–818. https://doi.org/10.1130/G39147.1

Goebel, T. H. W., Rosson, Z., Brodsky, E. E., & Walter, J. I. (2019). Aftershock deficiency of induced earthquake sequences during rapid mitigation efforts in Oklahoma. *Earth and Planetary Science Letters*, *522*, 135–143. https://doi.org/10.1016/j.epsl.2019.06.036

Gulia, L., & Wiemer, S. (2019). Real-time discrimination of earthquake foreshocks and aftershocks. *Nature*, *574*(7777), 193–199. https://doi.org/10.1038/s41586-019-1606-4

Gutenberg, B., & Richter, C. F. (1944). Frequency of earthquakes in California. *Bulletin of the Seismological Society of America*, *34*(4), 185–188. https://doi.org/10.1785/bssa0340040185

Hanks, T. C., & Kanamori, H. (1979). A moment magnitude scale. *Journal of Geophysical Research*, *84*(B5), 2348–2350. https://doi.org/10.1029/jb084ib05p02348

Hardebeck, J. L., & Shearer, P. M. (2002). A new method for determining first-motion focal mechanisms. *Bulletin of the Seismological Society of America*, *92*(6), 2264–2276. https://doi.org/10.1785/0120010200

Hastings, W. K. (1970). Monte Carlo sampling methods using Markov chains and their applications. *Biometrica*, *57*(1), 97–109. https://doi.org/10.1093/biomet/57.1.97

Hillers, G., Vuorinen, T. A. T., Uski, M. R., Kortström, J. T., Mäntyniemi, P. B., Tiira, T., et al. (2020). The 2018 geothermal reservoir stimulation in Espoo/Helsinki, Southern Finland: Seismic network anatomy and data features. *Seismological Research Letters*, *91*(2A), 770–786. https://doi.org/10.1785/0220190253

Hofmann, H., Zimmermann, G., Farkas, M., Huenges, E., Zang, A., Leonhardt, M., et al. (2019). First field application of cyclic soft stimulation at the Pohang Enhanced Geothermal System site in Korea. *Geophysical Journal International*, *217*(2), 926–949. https://doi.org/10.1093/gji/ggz058

Kagan, Y. Y. (2007). Simplified algorithms for calculating double-couple rotation. *Geophysical Journal International*, *171*(1), 411–418. https://doi.org/10.1111/j.1365-246x.2007.03538.x

Kaiser, J. (1953). Kenntnisse und Folgerungen aus der Messung von Geräuschen bei Zugbeanspruchung von metallischen Werkstoffen. *Arch. Für Isenhütten-Wesen*, *24*(1–2), 43–45. https://doi.org/10.1002/srin.195301381

Karimi, K., & Davidsen, J. (2021). Aftershock triggering and spatial aftershock zones in fluid-driven settings: Discriminating induced seismicity from natural swarms. *Geophysical Research Letters*, *48*(15), e2020GL092267. https://doi.org/10.1029/2020GL092267

Kroll, K. A., & Cochran, E. S. (2021). Stress controls rupture extent and maximum magnitude of induced earthquakes. *Geophysical Research Letters*, *48*(11), e2020GL092148. https://doi.org/10.1029/2020GL092148

Kwiatek, G., Bulut, F., Bohnhoff, M., & Dresen, G. (2014). High-resolution analysis of seismicity induced at Berlín geothermal field, El Salvador. *Geothermics*, *52*, 98–111. https://doi.org/10.1016/j.geothermics.2013.09.008

Kwiatek, G., Martínez-Garzón, P., & Bohnhoff, M. (2016). HybridMT: A MATLAB/shell environment package for seismic moment tensor inversion and refinement. *Seismological Research Letters*, *87*(4), 964–976. https://doi.org/10.1785/0220150251

Kwiatek, G., Martínez-Garzón, P., Dresen, G., Bohnhoff, M., Sone, H., & Hartline, C. (2015). Effects of long-term fluid injection on induced seismicity parameters and maximum magnitude in northwestern part of The Geysers geothermal field. *Journal of Geophysical Research: Solid Earth*, *120*, 7085–7101. https://doi.org/10.1002/2015JB012362

Kwiatek, G., Martínez-Garzón, P., & Karjalainen, A. (2022). Earthquake catalog of induced seismicity associated with 2020 hydraulic stimulation campaign at OTN-2 well in Helsinki, Finland. *GFZ Data Services*. https://doi.org/10.5880/GFZ.4.2.2022.001

Kwiatek, G., Plenkers, K., & Dresen, G. (2011). Source parameters of picoseismicity recorded at Mponeng deep gold mine, South Africa: Implications for scaling relations. *Bulletin of the Seismological Society of America*, *101*(6), 2592–2608. https://doi.org/10.1785/0120110094

Kwiatek, G., Plenkers, K., Nakatani, M., Yabe, Y., Dresen, G., & Group, J. (2010). Frequency-magnitude characteristics down to magnitude -4.4 for induced seismicity recorded at Mponeng Gold Mine, South Africa. *Bulletin of the Seismological Society of America*, *100*(3), 1167–1173. https://doi.org/10.1785/0120090277

Kwiatek, G., Saarno, T., Ader, T., Bluemle, F., Bohnhoff, M., Chendorain, M., et al. (2019). Controlling fluid-induced seismicity during a 6.1-km-deep geothermal stimulation in Finland. *Science Advances*, *5*(5), eaav7224. https://doi.org/10.1126/sciadv.aav7224

Langenbruch, C., Dinske, C., & Shapiro, S. A. (2011). Inter event times of fluid induced earthquakes suggest their Poisson nature. *Geophysical Research Letters*, *38*(21), L21302. https://doi.org/10.1029/2011GL049474

Lasocki, S., & Papadimitriou, E. E. (2006). Magnitude distribution complexity revealed in seismicity from Greece. *Journal of Geophysical Research: Solid Earth*, *111*, B11309. https://doi.org/10.1029/2005JB003794

Leonhardt, M., Kwiatek, G., Martínez-Garzón, P., Bohnhoff, M., Saarno, T., Heikkinen, P., & Dresen, G. (2021). Seismicity during and after stimulation of a 6.1 km deep enhanced geothermal system in Helsinki, Finland. *Solid Earth*, *12*(3), 581–594. https://doi.org/10.5194/se-12-581-2021

Leonhardt, M., Kwiatek, G., Martinez-Garzon, P., & Heikkinen, P. (2021). Earthquake catalogue of induced seismicity recorded during and after stimulation of Enhanced Geothermal System in Helsinki, Finland. *GFZ Data Serv*. https://doi.org/10.5880/GFZ.4.2.2021.001

Lord-May, C., Baró, J., Eaton, D. W., & Davidsen, J. (2020). Seismic hazard due to fluid injections. *Physical Review Research*, *2*(4), 043324. https://doi.org/10.1103/PhysRevResearch.2.043324

Maghsoudi, S., Baró, J., Kent, A., Eaton, D., & Davidsen, J. (2018). Interevent triggering in microseismicity induced by hydraulic fracturing. *Bulletin of the Seismological Society of America*, *108*(3A), 1133–1146. https://doi.org/10.1785/0120170368

Maghsoudi, S., Eaton, D. W., & Davidsen, J. (2016). Nontrivial clustering of microseismicity induced by hydraulic fracturing. *Geophysical Research Letters*, *43*(20), 10672–10679. https://doi.org/10.1002/2016GL070983

Main, I. G. (1991). A modified Griffith criterion for the evolution of damage with a fractal distribution of crack lengths: Application to seismic event rates and b-values. *Geophysical Journal International*, *107*(2), 353–362. https://doi.org/10.1111/j.1365-246X.1991.tb00830.x

Majer, E. L., Nelson, J., Robertson-Tait, A., Savy, J., & Wong, A. (2012). *Protocol for addressing induced seismicity associated with Enhanced Geothermal Systems*. U.S. Department of Energy. DOE/EE-0662.

Martínez-Garzón, P., Kwiatek, G., Bentz, S., Bohnhoff, M., & Dresen, G. (2020). Induced earthquake potential in geothermal reservoirs: Insights from The Geysers, California. *The Leading Edge*, *39*(12), 873–882. https://doi.org/10.1190/tle39120873.1

Martínez-Garzón, P., Kwiatek, G., Bohnhoff, M., & Dresen, G. (2017). Volumetric components in the earthquake source related to fluid injection and stress state. *Geophysical Research Letters*, *44*(2), 800–809. https://doi.org/10.1002/2016GL071963

Martínez-Garzón, P., Zaliapin, I., Ben-Zion, Y., Kwiatek, G., & Bohnhoff, M. (2018). Comparative study of earthquake clustering in relation to hydraulic activities at geothermal fields in California. *Journal of Geophysical Research: Solid Earth*, *123*, 4041–4062. https://doi.org/10.1029/2017JB014972

Maxwell, S. C. (2011). What does microseismic tell us about hydraulic fracture deformation. *CSEG Rec. - Focus Artic.*, *36*(8).

McGarr, A. (2014). Maximum magnitude earthquakes induced by fluid injection. *Journal of Geophysical Research: Solid Earth*, *119*(2), 1008–1019. https://doi.org/10.1002/2013JB010597

McGarr, A., & Barbour, A. J. (2018). Injection-induced moment release can also be aseismic. *Geophysical Research Letters*, *45*(11), 5344–5351. https://doi.org/10.1029/2018GL078422

McLaskey, G. C. (2019). Earthquake initiation from laboratory observations and implications for foreshocks. *Journal of Geophysical Research: Solid Earth*, *124*(12), 12882–12904. https://doi.org/10.1029/2019jb018363

Meredith, P. G., & Atkinson, B. K. (1983). Stress corrosion and acoustic emission during tensile crack propagation in Whin Sill dolerite and other basic rocks. *Geophysical Journal International*, *75*(1), 1–21. https://doi.org/10.1111/j.1365-246X.1983.tb01911.x

Metropolis, N., Rosenbluth, A., Rosenbluth, M., Teller, A., & Teller, E. (1953). Equation of state calculations by fast computing machines. *Journal of Chemical Physics*, *21*(6), 1087–1092. https://doi.org/10.1063/1.1699114

Michailos, K. (2019). Southern Alps, New Zealand microseismicity earthquake catalogue. https://doi.org/10.5281/zenodo.3529755

Michailos, K., Smith, E. G. C., Chamberlain, C. J., Savage, M. K., & Townend, J. (2019). Variations in seismogenic thickness along the Central Alpine Fault, New Zealand, revealed by a Decade's relocated microseismicity. *Geochemistry, Geophysics, Geosystems*, *20*(1), 470–486. https://doi.org/10.1029/2018gc007743

Mignan, A., Broccardo, M., & Wang, Z. (2021). Comprehensive survey of seismic hazard at geothermal sites by a meta-analysis of the underground feedback activation parameter afb. *Energies*, *14*(23), 7998. https://doi.org/10.3390/en14237998

Mignan, A., Broccardo, M., Wiemer, S., & Giardini, D. (2017). Induced seismicity closed-form traffic light system for actuarial decision-making during deep fluid injections. *Scientific Reports*, *7*(1), 13607. https://doi.org/10.1038/s41598-017-13585-9

Passelègue, F. X., Brantut, N., & Mitchell, T. M. (2018). Fault reactivation by fluid injection: Controls from stress state and injection rate. *Geophysical Research Letters*, *45*(23), 12837–12846. https://doi.org/10.1029/2018GL080470

Rintamäki, A. E., Hillers, G., Vuorinen, T. A. T., Luhta, T., Pownall, J. M., Tsarsitalidou, C., et al. (2021). A seismic network to monitor the 2020 EGS stimulation in the Espoo/Helsinki Area, Southern Finland. *Seismological Research Letters*, *93*(2A), 1046–1062. https://doi.org/10.1785/0220210195

Rudnicki, J. W., & Zhan, Y. (2020). Effect of pressure rate on rate and state frictional slip. *Geophysical Research Letters*, *47*(21), e2020GL089426. https://doi.org/10.1029/2020GL089426

Rydelek, P. A., & Sacks, I. S. (1989). Testing the completeness of earthquake catalogues and the hypothesis of self-similarity. *Nature*, *337*(6204), 251–253. https://doi.org/10.1038/337251a0

Schoenball, M., Baujard, C., Kohl, T., & Dorbath, L. (2012). The role of triggering by static stress transfer during geothermal reservoir stimulation. *Journal of Geophysical Research: Solid Earth*, *117*, B09307. https://doi.org/10.1029/2012JB009304

Schoenball, M., Davatzes, N. C., & Glen, J. M. G. (2015). Differentiating induced and natural seismicity using space-time-magnitude statistics applied to the Coso Geothermal field. *Geophysical Research Letters*, *42*(15), 6221–6228. https://doi.org/10.1002/2015GL064772

Scholz, C. H. (1968). The frequency-magnitude relation of microfracturing in rock and its relation to earthquakes. *Bulletin of the Seismological Society of America*, *58*(1), 399–415. https://doi.org/10.1785/bssa0580010399

Schorlemmer, D., Wiemer, S., & Wyss, M. (2005). Variations in earthquake-size distribution across different stress regimes. *Nature*, *437*(7058), 539–542. https://doi.org/10.1038/nature04094

Shapiro, S. A., Dinske, C., Langenbruch, C., & Wenzel, F. (2010). Seismogenic index and magnitude probability of earthquakes induced during reservoir fluid stimulations. *The Leading Edge*, *29*(3), 304–309. https://doi.org/10.1190/1.3353727

Shen, L. W., Schmitt, D. R., Wang, R., & Hauck, T. E. (2021). States of in situ stress in the Duvernay East Shale Basin and Willesden Green of Alberta, Canada: Variable in situ stress states effect fault stability. *Journal of Geophysical Research: Solid Earth*, *126*, e2020JB021221. https://doi.org/10.1029/2020JB021221

Shi, Y., & Bolt, B. A. (1982). The standard error of the magnitude-frequency b value. *Bulletin of the Seismological Society of America*, *72*(5), 1677–1687. https://doi.org/10.1785/BSSA0720051677

Stierle, E., Vavryčuk, V., Šílený, J., & Bohnhoff, M. (2014). Resolution of non-double-couple components in the seismic moment tensor using regional networks—I: A synthetic case study. *Geophysical Journal International*, *196*(3), 1869–1877. https://doi.org/10.1093/gji/ggt502

Uski, M., Lund, B., & Oinonen, K. (2015). Scaling relations for homogeneous moment based magnitude. In J. Saari, B. Lund, M. Malm, P. Mäntyniemi, K. Oinonen, T. Tiira, et al. (Eds.), *Evaluating seismic hazard for the hanhikivi nuclear power plant site. Seismological characteristics of the seismic source areas, attenuation of seismic signal, and probabilistic analysis of seismic hazard* (p. 125) Report NE-4459. ÅF-Consult Ltd.

Uski, M., & Tuppurainen, A. (1996). A new local magnitude scale for the Finnish seismic network. *Seismic Source Parameters: From Microearthquakes to Large Events*, *261*(1), 23–37. https://doi.org/10.1016/0040-1951(96)00054-6

Utsu, T. (1961). A statistical study on the occurrence of aftershocks. *Geophysical Magazine*, *30*, 521–605.

Utsu, T. (1965). A method for determining b in a formula log(N)=a-bM showing the magnitude-frequency distribution of earthquakes. *Geophysical Bulletin of Hokkaido University*, *13*, 99–103.

van der Elst, N. J., & Brodsky, E. E. (2010). Connecting near-field and far-field earthquake triggering to dynamic strain. *Journal of Geophysical Research: Solid Earth*, *115*, B07311. https://doi.org/10.1029/2009JB006681

van der Elst, N. J., Page, M. T., Weiser, D. A., Goebel, T. H. W., & Hosseini, S. M. (2016). Induced earthquake magnitudes are as large as (statistically) expected. *Journal of Geophysical Research: Solid Earth*, *121*, 4575–4590. https://doi.org/10.1002/2016JB012818

Verdecchia, A., Cochran, E. S., & Harrington, R. M. (2021). Fluid-earthquake and earthquake-earthquake interactions in Southern Kansas, USA. *Journal of Geophysical Research: Solid Earth*, *126*, e2020JB020384. https://doi.org/10.1029/2020JB020384

Waldhauser, F., & Ellsworth, W. L. (2000). A double-difference earthquake location algorithm: Method and application to the Northern Hayward Fault, California. *Bulletin of the Seismological Society of America*, *90*(6), 1353–1368. https://doi.org/10.1785/0120000006

Wang, L., Kwiatek, G., Rybacki, E., Bohnhoff, M., & Dresen, G. (2020). Injection-induced seismic moment release and laboratory fault slip: Implications for fluid-induced seismicity. *Geophysical Research Letters*, *47*(22), e2020GL089576. https://doi.org/10.1029/2020GL089576

Wang, L., Kwiatek, G., Rybacki, E., Bonnelye, A., Bohnhoff, M., & Dresen, G. (2020). Laboratory study on fluid-induced fault slip behavior: The role of fluid pressurization rate. *Geophysical Research Letters*, *47*(6), e2019GL086627. https://doi.org/10.1029/2019GL086627

Weingarten, M., Ge, S., Godt, J. W., Bekins, B. A., & Rubinstein, J. L. (2015). High-rate injection is associated with the increase in U.S. mid-continent seismicity. *Science*, *348*(6241), 1336–1340. https://doi.org/10.1126/science.aab1345

Wiemer, S., & Wyss, M. (2000). Minimum magnitude of completeness in earthquake catalogs: Examples from Alaska, the Western United States & Japan. *Bulletin of the Seismological Society of America*, *90*(4), 859–869. https://doi.org/10.1785/0119990114

Yeo, I. W., Brown, M. R. M., Ge, S., & Lee, K. K. (2020). Causal mechanism of injection-induced earthquakes through the Mw 5.5 Pohang earthquake case study. *Nature Communications*, *11*(1), 2614. https://doi.org/10.1038/s41467-020-16408-0